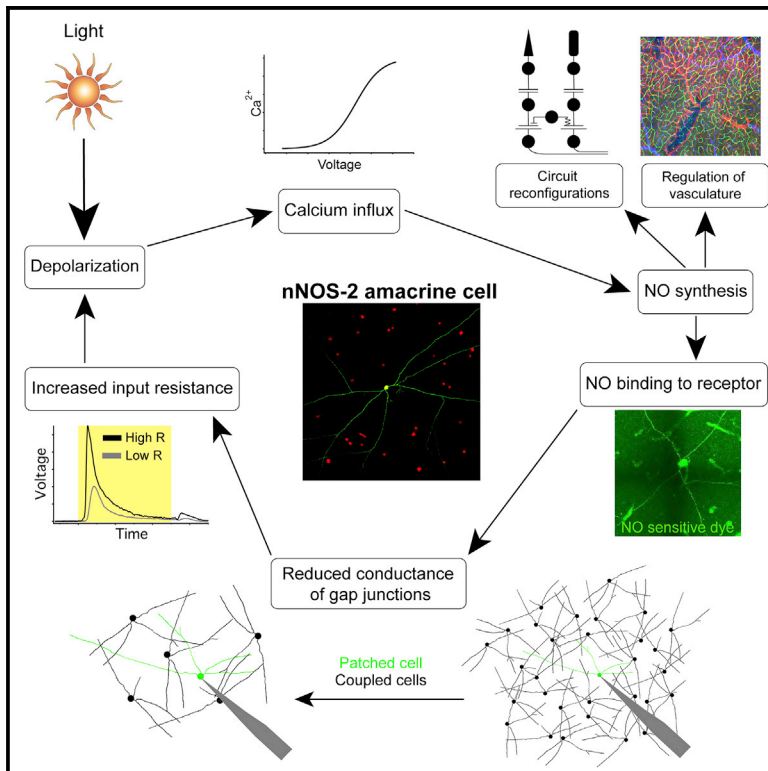


# Neuron

## A Self-Regulating Gap Junction Network of Amacrine Cells Controls Nitric Oxide Release in the Retina

### Graphical Abstract



### Authors

Jason Jacoby, Amurta Nath,  
Zachary F. Jessen,  
Gregory W. Schwartz

### Correspondence

greg.schwartz@northwestern.edu

### In Brief

Jacoby et al. show that a single amacrine cell type, the nNOS-2 AC, controls nitric oxide (NO) release in the retina. nNOS-2 ACs are electrically coupled in the dark and decouple in the light by sensing their own NO release.

### Highlights

- nNOS-2 amacrine cells are the main source of nitric oxide (NO) in the inner retina
- These cells release NO rapidly upon light-induced depolarization
- nNOS-2 amacrine cells are electrically coupled in the dark and decouple with NO
- This network demonstrates a new auto-regulation mechanism for NO release



# A Self-Regulating Gap Junction Network of Amacrine Cells Controls Nitric Oxide Release in the Retina

Jason Jacoby,<sup>1</sup> Amurta Nath,<sup>2,3</sup> Zachary F. Jessen,<sup>4</sup> and Gregory W. Schwartz<sup>1,5,6,7,\*</sup>

<sup>1</sup>Department of Ophthalmology, Northwestern University, Chicago, IL, USA

<sup>2</sup>Interdepartmental Neuroscience Program, Northwestern University, Chicago, IL, USA

<sup>3</sup>Interdepartmental Neuroscience Program, Northwestern University, Evanston, IL, USA

<sup>4</sup>Medical Scientist Training Program, Northwestern University, Chicago, IL, USA

<sup>5</sup>Department of Physiology, Feinberg School of Medicine, Northwestern University, Chicago, IL, USA

<sup>6</sup>Department of Neurobiology, Weinberg College of Arts and Sciences, Northwestern University, Evanston, IL, USA

<sup>7</sup>Lead Contact

\*Correspondence: [greg.schwartz@northwestern.edu](mailto:greg.schwartz@northwestern.edu)

<https://doi.org/10.1016/j.neuron.2018.09.047>

## SUMMARY

Neuromodulators regulate circuits throughout the nervous system, and revealing the cell types and stimulus conditions controlling their release is vital to understanding their function. The effects of the neuromodulator nitric oxide (NO) have been studied in many circuits, including in the vertebrate retina, where it regulates synaptic release, gap junction coupling, and blood vessel dilation, but little is known about the cells that release NO. We show that a single type of amacrine cell (AC) controls NO release in the inner retina, and we report its light responses, electrical properties, and calcium dynamics. We discover that this AC forms a dense gap junction network and that the strength of electrical coupling in the network is regulated by light through NO. A model of the network offers insights into the biophysical specializations leading to auto-regulation of NO release within the network.

## INTRODUCTION

Nitric oxide (NO) has modulatory functions in many neuronal and neurovascular circuits (Garthwaite, 2008). In the retina, its effects have been most closely associated with circuit reconfigurations to support transitions across light levels. NO increases the gain of cone synapses in the outer retina (Snellman and Nawy, 2004) and acts through a variety of pathways in the inner retina. NO has been shown to reduce the conductance of gap junctions between All amacrine cells and cone bipolar cells that are required for scotopic signals (Mills and Massey, 1995) and increase the gain of cone bipolar cell synapses that carry photopic signals (Tooker et al., 2013; Vielma et al., 2014). Mice lacking the neuronal NO synthase (nNOS) enzyme exhibit deficiencies in photopic responses (Wang et al., 2007).

Despite much information about the effects of NO in the retina, very little is known about the cells and stimulus conditions con-

trolling its release, primarily because we have lacked measurements from NO-releasing amacrine cells (ACs) (NOACs). Dopamine is another neuromodulator involved in light adaptation in the retina, and our understanding of dopaminergic ACs provides a point of comparison for the differences between these two modulators and the gaps in our knowledge about NO release. Dopamine levels in the retina fluctuate gradually with the circadian cycle (Nir et al., 2000). Dopaminergic ACs are tonically spiking (Puopolo et al., 2001; Zhang et al., 2007), and increases in their firing rate in response to changes in luminance have been linked to their synaptic connections with intrinsically photosensitive retinal ganglion cells (RGCs) (Berson et al., 2002; Hattar et al., 2003). In contrast, NO levels measured either *in vivo* or *in vitro* increase rapidly under photopic conditions, and flickering light is more effective than constant illumination at triggering NO release (Blom et al., 2012; Eldred and Blute, 2005; Neal et al., 1998; Vielma et al., 2010; Wang et al., 2007). Functional measurements from NOACs would provide insights into the dynamic control of NO and the mechanisms by which it differs from dopamine.

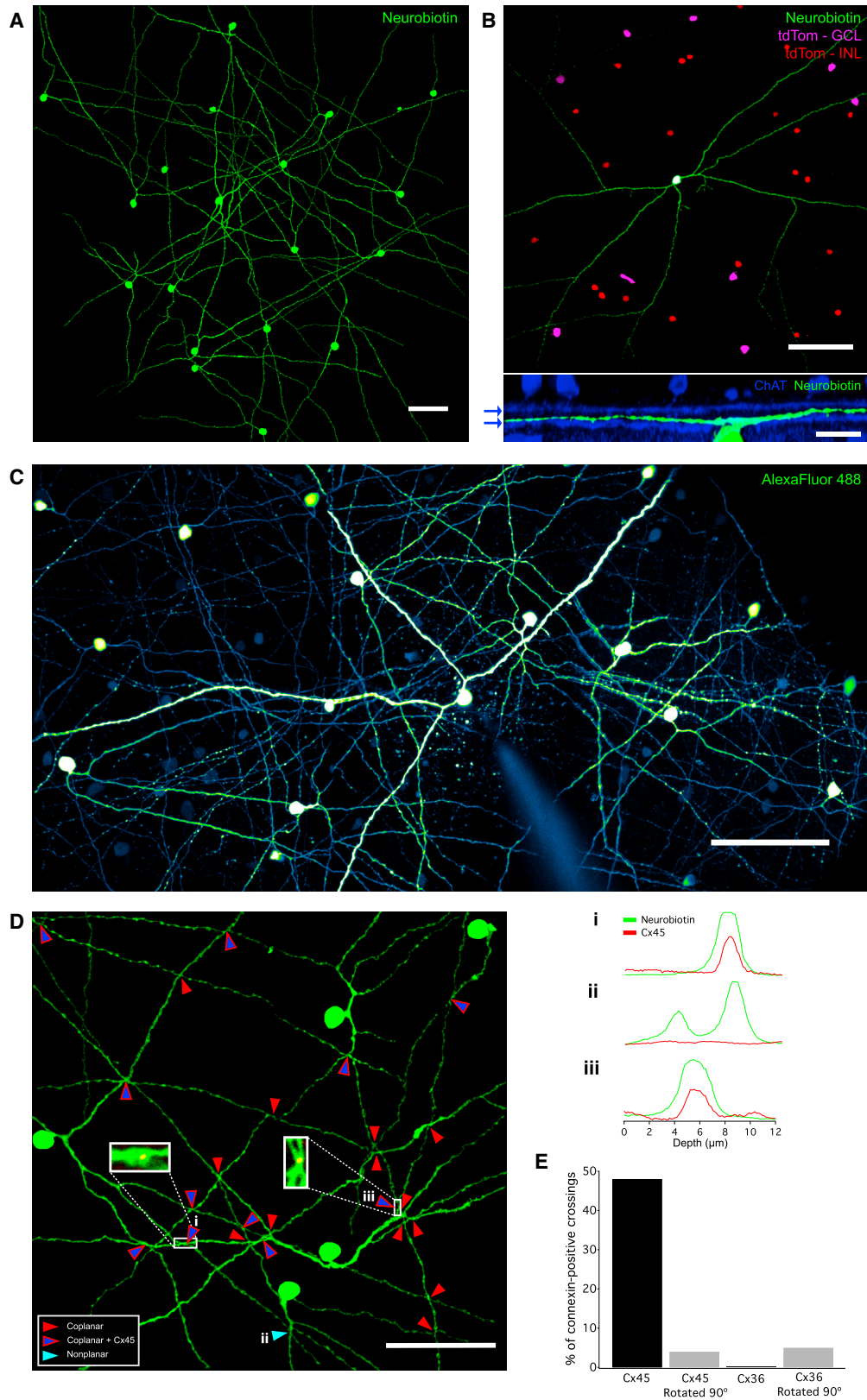
We show that a single NOAC, called the nNOS-2 AC, dominates NO production in the inner retina; depolarizing single nNOS-2 ACs leads to NO release. We report the light responses, electrical properties, and calcium dynamics that drive NO release in these cells. The most striking feature of nNOS-2 ACs is that they are massively and homologously coupled in a dense gap junction network. We discovered that coupling strength in the nNOS-2 AC network is dynamically regulated by light and can alter the input resistance of the ACs. Light-driven decoupling in the nNOS-2 network relies on NO, constituting a self-regulatory loop. Using a biophysical model of the nNOS-2 AC network, we explore the specializations in the nNOS-2 AC circuit, like high neurite resistivity and large gap junction conductance, that enable decoupling to alter network excitability.

## RESULTS

### nNOS-2 ACs Form a Dense Gap Junction Network

We used the nNOS-Cre transgenic mouse line to target NOACs for physiological and morphological measurements. A previous





(legend on next page)

study identified two morphological types of ACs labeled in this line (Zhu et al., 2014). Although nNOS-1 ACs resemble a spiking polyaxonal cell type termed the A1 AC (Badea and Nathans, 2004; Famiglietti, 1992; Stafford and Dacey, 1997), we focused on nNOS-2 ACs because they morphologically resemble cells that have been characterized as immunoreactive for nNOS in the rat retina (Pang et al., 2010), but nothing is known about their physiology in mouse. We targeted nNOS-2 ACs under two-photon laser illumination and identified them by fluorescence labeling (tdTomato expression in the Ai9 reporter line). Although nNOS-2 ACs were the minority of cells in the ganglion cell layer (GCL) labeled in this line, we used their characteristic morphology to target them for whole-cell recordings. A single neurite “neck” emanates from the soma of the nNOS-2 AC and bifurcates near the middle of the inner plexiform layer (IPL).

In initial experiments to characterize the morphology of nNOS-2 ACs, we filled the cells with neurobiotin. A single nNOS-2 AC filled with neurobiotin under dark conditions revealed a vast gap junction network of morphologically similar cells (Figure 1A;  $44 \pm 3$  coupled cells,  $n = 6$  injections from different retinas). Among all coupled cells,  $7\% \pm 0.3\%$  were located in the GCL, whereas  $93\% \pm 2\%$  were located in the inner nuclear layer (INL) (16 GCL somata + 201 INL somata from 217 total coupled nNOS-2 ACs counted;  $n = 5$  retinas). In addition to their similar morphology, every coupled cell was both positive for tdTomato in the nNOS-Cre reporter line and positive for an antibody against nNOS (Figure S1), providing additional evidence that the coupled network only included nNOS-2 ACs. Blocking gap junctions with meclofenamic acid (MFA) allowed us to reconstruct the morphology of individual nNOS-2 ACs. The reconstructed single cells had long, very sparsely branching neurites in the middle of the IPL, consistent with a previous report (Figure 1B; Zhu et al., 2014).

Remarkably, gap junctions between nNOS-2 ACs passed not only the small tracer molecule neurobiotin (322 g/mol) but also passed Alexa Fluor 488, a molecule of nearly twice the molecular weight (580 g/mol; Figure 1C). The large molecule permeability and extent of the filled network suggested a very large gap-junctional conductance and was further explored in experiments and modeling below. We used antibodies to different connexin proteins to determine which subtypes form the structural hemichannels in the nNOS-2 AC network. Connexin 36 (Cx36) and Cx45 are both prevalent in the inner retina (Figures S2B and S2C), so we tested for the presence of both hemichannel proteins at crossings between nNOS-2 AC neurites. Cx36 was not observed

at these crossings (Figure S2A), but Cx45 was indeed present (Figure 1D). We observed Cx45 puncta in 48% (11 of 23) of putatively “touching” neurites (that crossed within the same focal plane) (Figures 1Di and 1Diii). Neurites that did not touch (4–12  $\mu\text{m}$  separation in the z axis) showed either a complete absence of puncta or Cx45 puncta registered in a different plane (Figure 1Dii). Rotating the Cx45 channel in the image by  $90^\circ$  as a negative control eliminated all but one of the colocalized puncta (Figure 1E). Under the assumption that the Cx45-containing crossings represent gap junctions, we estimate their density to be  $\sim 200/\text{mm}^2$ .

We tested for functional coupling between nNOS-2 ACs using paired recordings (Figure 2). We used Alexa Fluor 488 permeability to help us identify coupled cells and target them for paired recordings. When an nNOS-2 AC in the GCL was patched and filled with Alexa Fluor 488, a neighboring soma in the GCL could be targeted using two-photon fluorescence and patched with a second electrode (Figure 2A; STAR Methods). A total of 4 nNOS-2 AC pairs were recorded, and each pair showed bidirectional electrical coupling with a characteristically linear current-voltage function passing through the origin (Figures 2B–2D). Gap junctions between nNOS-2 ACs showed little voltage dependence in their conductance because the trans-junctional current-voltage relationship was linear over the physiological range of membrane potential fluctuations of the injected cell (Figures 2B–2D). The coupling coefficient measured with somatic current injections was  $7.5\% \pm 0.4\%$ , with a shallow dependence on the distance between somata (Figure 2E).

### nNOS-2 ACs Depolarize Transiently for Bright Stimuli

To assess their light responses, we recorded nNOS-2 ACs in current clamp configuration. These cells had a resting membrane potential of  $-61 \pm 2$  mV ( $n = 16$ ) in darkness. Upon presentation of a light spot of 200 rod isomerizations ( $R^*$ )/rod/s, measuring 200  $\mu\text{m}$  in diameter, nNOS-2 ACs depolarized by  $28 \pm 1$  mV ( $n = 16$ ) at light onset (Figure 3A). We then recorded their responses to light steps of 100% contrast across a range of light levels (Figure 3B). With steps of increasing luminance, their responses increased in amplitude, decreased in latency, and developed an OFF response (Figures 3B and 3C).

Despite wide-field morphology typical of spiking ACs, we never observed action potentials in nNOS-2 ACs, either with light stimuli or with depolarizing current injections (Figure 3D).

### Figure 1. nNOS-2 ACs Form a Dense Electrically Coupled Network via Connexin 45 Hemichannels

- (A) Network coupling from a single nNOS-2 AC filled with neurobiotin. Scale bar, 100  $\mu\text{m}$ .
- (B) Top: morphology of an nNOS-2 AC filled with neurobiotin (green) in an nNOS-Cre transgenic retina in the presence of MFA; Ai9 reporter-driven expression of tdTomato is observed in both GCL (magenta) and INL (red) somata. Scale bar, 100  $\mu\text{m}$ . Bottom: side view showing stratification with ChAT bands (blue); the location is marked with blue arrows. Scale bar, 20  $\mu\text{m}$ .
- (C) Alexa Fluor 488 readily passes through nNOS-2 AC gap junctions. Multi-photon Z projection image of an nNOS-2 gap junction-coupled network, revealed after a single nNOS-2 AC was patched and filled with Alexa Fluor 488. Scale bar, 100  $\mu\text{m}$ .
- (D) Projection image depicting coplanar crossings (red triangles), coplanar crossings with Cx45 puncta present (blue triangles outlined in red), and a single nonplanar crossing (cyan) to represent neurites offset in the z axis. Scale bar, 50  $\mu\text{m}$ . The numbered crossings (i)–(iii) are graphed below the image z axis profile of neurobiotin-filled neurite channel (green) and Cx45 antibody channel (red). Graphs (i) and (iii) depict Cx45 positive, coplanar crossings and are visualized in the inset images (white boxes), with colocalization between the neurobiotin channel and Cx45 channel yielding a single yellow punctum (the long side of the images measures 5.4  $\mu\text{m}$ ). Graph (ii) shows two distinct neurobiotin peaks (nonplanar) and an absence of Cx45 in both offset neurites.
- (E) Black bars represent the percentage of coplanar crossings that contain Cx45 puncta (48%, 11 of 23) and Cx36 puncta (0%, 0 of 20); the gray bars represent the percentage of coplanar crossings that contain Cx45 puncta (4%, 1 of 23) or Cx36 puncta (5%, 1 of 20) when the connexin channel was rotated 90 degrees.

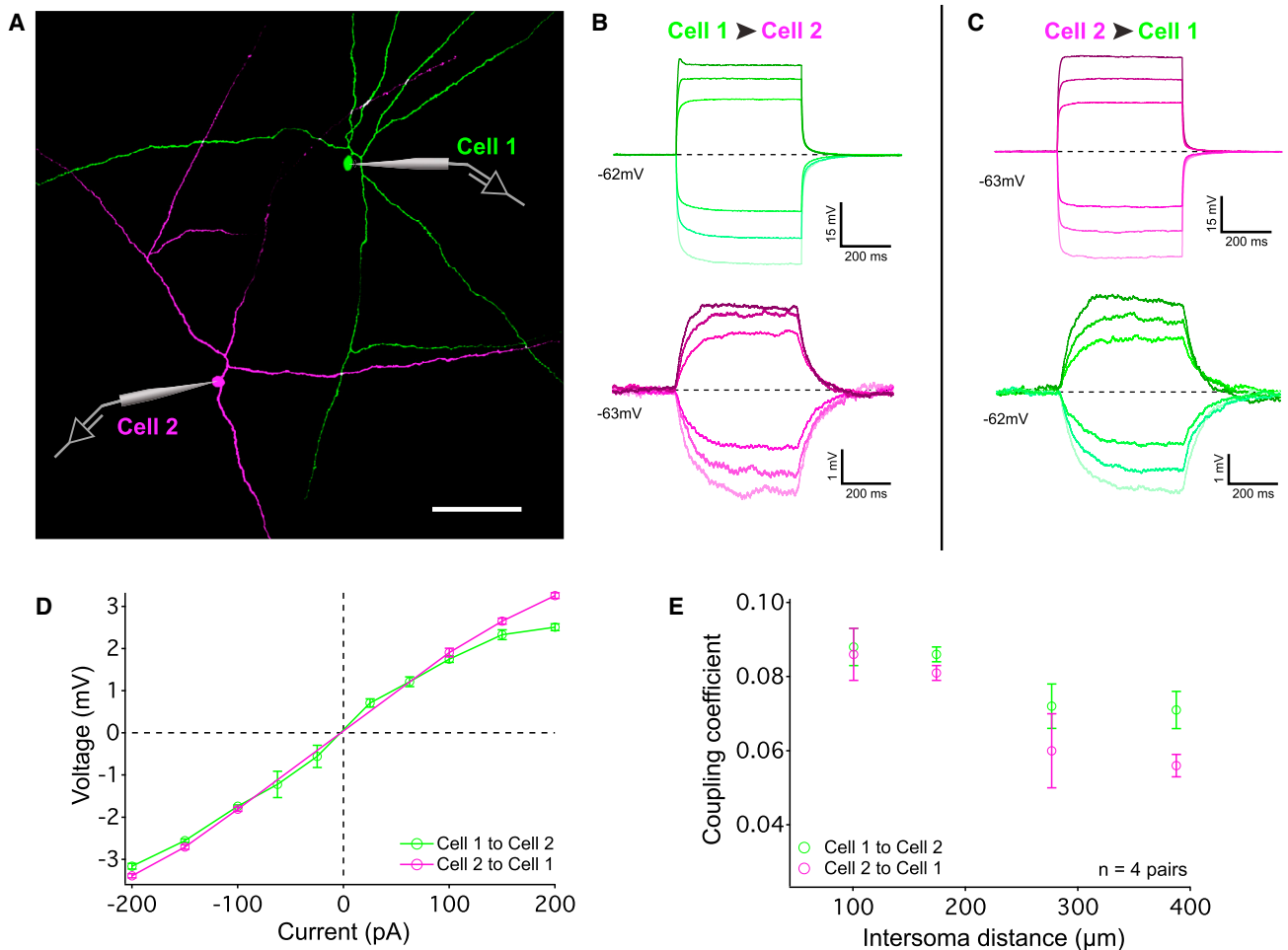


**Figure 2. Direct Measurements of Gap Junction Conductance by Paired Recordings**

(A) Traced image showing a recorded pair of gap-junctionally coupled nNOS-2 ACs. Scale bar, 100  $\mu\text{m}$ .

(B) Membrane voltage changes in cell 1 (green traces) and cell 2 (magenta traces) resulting from current injections in cell 1. Dotted lines indicate the resting membrane potential.

(C) The same as in (B), but current injections are in cell 2. Average traces of 10 individual trials are shown for (B) and (C).

(D) Current-voltage relationship for the electrically coupled cells in (A). Error bars indicate SEM across trials ( $n = 5$  trials).

(E) Coupling coefficient versus intersoma distance. Data points are each direction of injections for each of the 4 cell pairs. Error bars indicate SEM across  $n = 8$  different amplitude (positive and negative) current injections as in (D).

Although the resting membrane potential of nNOS-2 ACs adapted rapidly to steps in mean illumination, the cell responded robustly to a photopic stimulus flickering at 3 Hz (Figure 3E), a paradigm previously shown to elicit NO release in the retina (Blom et al., 2012; Eldred and Blute, 2005).

#### Depolarization Causes Calcium Influx in nNOS-2 AC Neurites

NO synthesis is initiated in nNOS-expressing neurons via direct interaction of calcium with nNOS-bound calmodulin following depolarization (McMurry et al., 2011; Tricoire and Vitalis, 2012) and, thus, is blocked by buffering calcium with sufficiently high levels of EGTA (Garthwaite et al., 1988). Unlike traditional neurotransmitters, NO diffuses freely across cell membranes, so its release depends only on its rate of synthesis (Garthwaite,

2008). We sought to measure the voltage dependence of calcium influx in nNOS-2 ACs to give us insights into the conditions under which the light-evoked depolarizations we measured could lead to NO release. There are, of course, possible sources of calcium influx into nNOS-2 ACs other than voltage-gated calcium channels (like N-methyl D-aspartate [NMDA] receptors or calcium-permeable AMPA receptors), but we focused on the voltage-driven calcium influx because we could isolate the currents pharmacologically from any possible network effects of receptor blockers, and we measured robust signals in the physiological voltage range of the cell that are likely responsible for the majority of light-driven calcium influx.

In the first set of experiments, we depolarized nNOS-2 ACs with current injections and measured changes in the fluorescence of the calcium indicator Oregon Green BAPTA-1 (OGB-1)

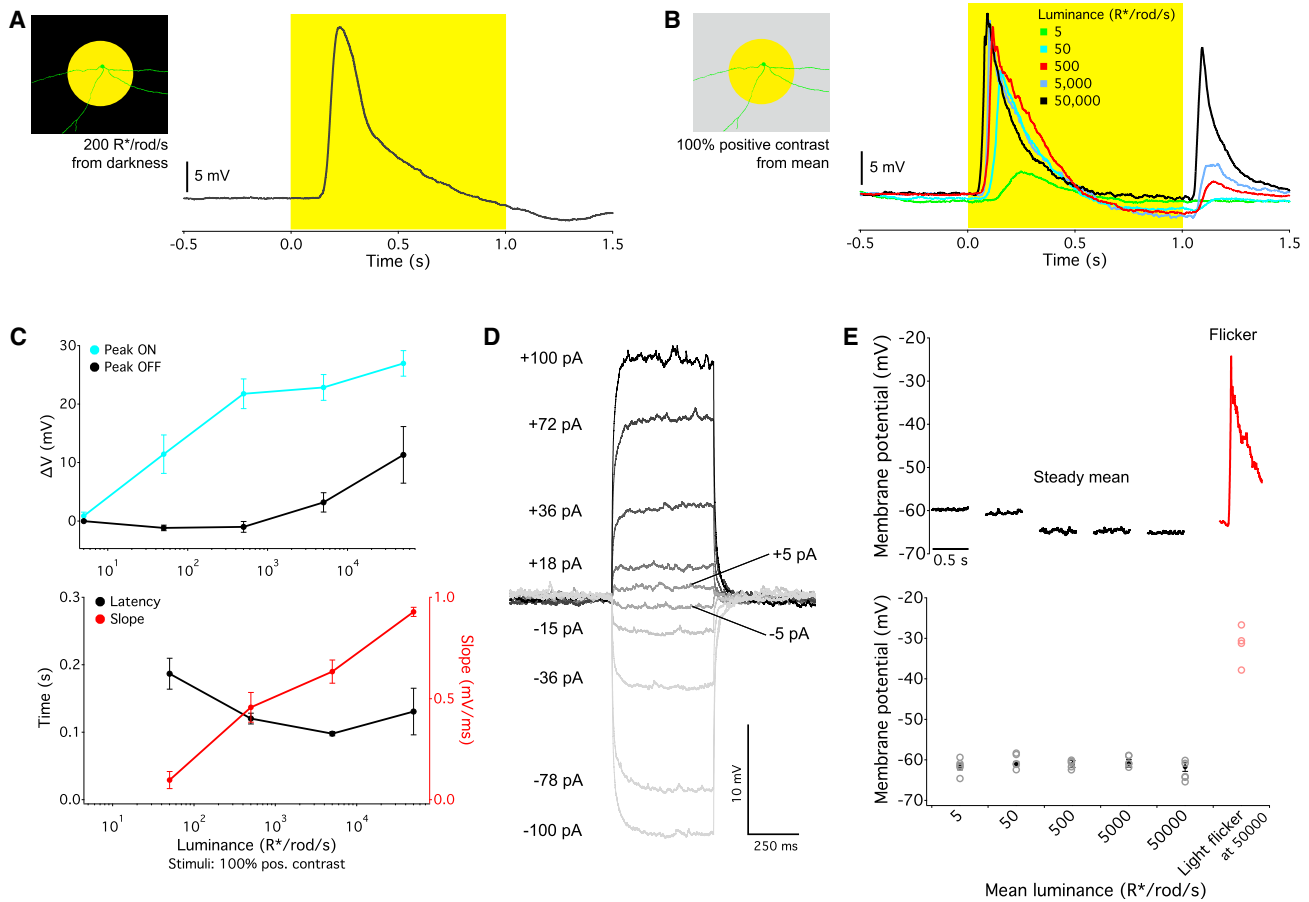


### Figure 3. Physiology of nNOS-2 ACs

(A) Representative current clamp recording of an nNOS-2 AC in response to a light spot (200  $\mu\text{m}$  diameter, 200  $\text{R}^*/\text{rod/s}$ ) from darkness. (B) Membrane potential changes in response to stimuli of increasing light levels; 100% positive Weber contrast spots are presented. Average traces from 10 individual trials are shown for (C) and (D). (C) Top: peak ON (cyan) and OFF (black) response amplitudes of nNOS-2 ACs stimulated at 100% positive Weber contrast. Bottom: changes in kinetics of both response latency (black trace, left axis) and slope (red trace, right [red] axis) derived from responses across light levels as shown in (B). Error bars indicate SEM across cells ( $n = 4$ ). (D) Single-trial raw traces from a current injection series from a recorded nNOS-2 AC. (E) Top: baseline membrane potential measured before light stimulation at different mean background illumination levels (black traces). Shown is the cycle average response of an nNOS-2 AC to a 3-Hz light flicker at 50,000  $\text{R}^*/\text{rod/s}$  (red trace). Bottom: population average of baseline membrane potentials (black) and peak response to light flicker (red). Error bars indicate SEM across cells ( $n = 5$ ).

(Figure 4A). Unlike in spiking neurons, calcium changes were absent at the somata but were apparent in the neurites (Figures 4B and 4C). We chose a proximal location on the primary neurite where we observed maximal response amplitude and elicited a series of depolarizations in current clamp configuration. Our measurements revealed a steep, nonlinear dependence of calcium influx on voltage with a high activation threshold (Figure 4D; half-maximal voltage [ $V_{\text{half}}$ ] =  $-27.4 \pm 0$  mV, slope =  $6.1 \pm 0$ ,  $n = 3$ ).

In a second set of experiments, we measured  $\text{Ca}^{2+}$  currents in nNOS-2 ACs. We voltage-clamped the cells and measured their current-voltage relationships under control conditions (in the presence of synaptic blockers) and in the presence of cobalt (5 mM) to block  $\text{Ca}^{2+}$  currents (Figures 4E and 4F). We then subtracted the current traces in cobalt from those in the control to isolate  $\text{Ca}^{2+}$  currents driven through voltage-gated channels

by our depolarizations (Raman and Bean, 1999; Surprenant et al., 1990). Because of their wide-field morphology and the extensive coupling between nNOS-2 ACs, space-clamp issues were likely present in these voltage-clamp experiments. However, the effects of poor space-clamping in measuring voltage-dependent calcium currents are mitigated by the fact that the well-clamped channels in the proximal neurites (the same place we measured in our imaging experiments) are the ones providing most of the current. The large coupling coefficients measured in pairs of cells hundreds of microns apart (Figure 2E) also suggest that nNOS-2 ACs have an unusually long electrotonic length constant, as confirmed by the modeling results below.

Despite the technical differences between our two calcium measurements and the caveats of voltage-clamping in these

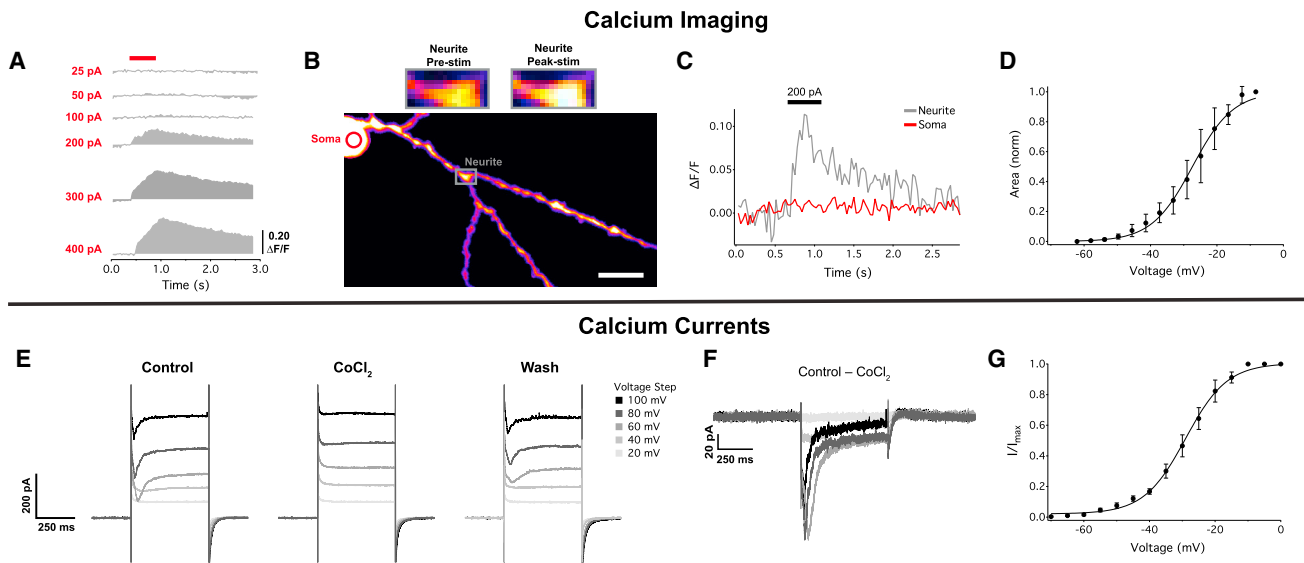


**Figure 4. Calcium Dynamics of nNOS-2 ACs**

(A) Gray traces depict the OGB-1 fluorescence change in response to current injections of increasing amplitude. The red bar indicates the duration of current injection.

(B) Two-photon fluorescent image showing OGB-1-filled nNOS-2 ACs; the gray traces on the left were derived from the region boxed in gray. Pre-stimulus and peak stimulus fluorescence change in primary neurites are depicted at the top. Scale bar, 10  $\mu$ m.

(C) Single traces of change in OGB-1 fluorescence in the soma (red) and neurite (gray) following 200 pA current injection. Regions of interests (ROIs) are marked in (B) with a red circle (soma) and gray square (neurite).

(D) Population data of the normalized area measured beneath functional calcium traces plotted versus the voltage response to current injection in various amplitudes, characterizing the fluorescence-to-voltage relationship. Error bars depict SEM across  $n = 3$  cells, with sigmoid fit shown in black.

(E) Currents recorded via voltage step pulse protocol under control conditions (left), during cobalt blockade of calcium channels (center), and following washoff (right).

(F) Difference currents between cobalt traces subtracted from control traces during the voltage step amplitudes shown in the legend.

(G) Population data of the normalized peak current (calcium) versus the voltage change of nNOS-2 ACs characterizing the direct calcium current-to-voltage relationship. Error bars depict SEM across  $n = 3$  cells, with sigmoid fit shown in black.

cells, the measurements agreed remarkably well in the shape of the activation curve (Figure 4G; Figures S3A and S3B; for calcium currents,  $V_{\text{half}} = -29.6 \pm 0.2$  mV, slope =  $6.6 \pm 0$ ,  $n = 3$ ). Calcium currents showed fast inactivation with a decay time constant of less than 70 ms (Figures S3C and S3D). Based on these activation curves, a substantial ( $\sim 30$  mV) depolarization is required for large calcium influx. This may serve as a thresholding mechanism so that calcium entry only occurs for large light responses, such as those elicited by bright flicker (Figure 3F; Discussion).

#### Depolarizing a Single nNOS-2 AC Releases NO

To test directly whether nNOS-2 ACs release NO, we injected current into individual cells during whole-cell recordings in the presence of the unipolar, NO-sensitive, fluorescent dye 4-amino-5-methylamino-2',7'-difluorofluorescein diacetate (DAF) (Kojima et al., 1999; Figure 5). Whole retinas were bath-loaded by incubation in DAF-containing solution, resulting in DAF being taken up by the entire retinal cell matrix. DAF only becomes fluorescent when it is exposed to NO and does not diminish unless bleached; stained tissue that is not exposed to NO remains non-fluorescent. Of note, both stimulated and unstimulated conditions were used in parallel, with a cell patched in one half of a retinal whole mount receiving current injection pulses, whereas a cell patched in the

other half of the retina was left unstimulated. Using confocal microscopy, we observed a sharp increase in NO levels (via increases in DAF fluorescence) both in the soma and neurites of the injected nNOS-2 AC as well as in nearby somata of coupled cells via depolarization through gap junction coupling. All somata labeled by DAF were also labeled by neurobiotin and tdTomato in the nNOS-Cre reporter line, confirming their identity as nNOS-2 ACs (Figure 5A). We quantified the spatial decay of the DAF signal both in coupled somata (Figure 5C) and in the neurites of the injected cell (Figure 5D). The decays were well fit by single exponentials with length constants of 130  $\mu$ m for somata and 303  $\mu$ m for neurites. The presence of brightly labeled blood vessels provides evidence that DAF was indeed measuring NO because the vascular epithelium releases its own NO through endothelial NOS (eNOS). We repeated these experiments in perforated patch configuration to ensure that we were not unphysiologically altering the calcium buffering capacity in nNOS-2 ACs. Cells depolarized in perforated patch ( $n = 2$ ) elicited similar NO responses as the cells depolarized in whole-cell configuration.

Experiments were performed in heterozygous mice in which Cre was knocked into the nNOS locus, so these animals are expected to have less nNOS than wild-type (WT) mice. Therefore, this widespread NO release upon depolarization of a single

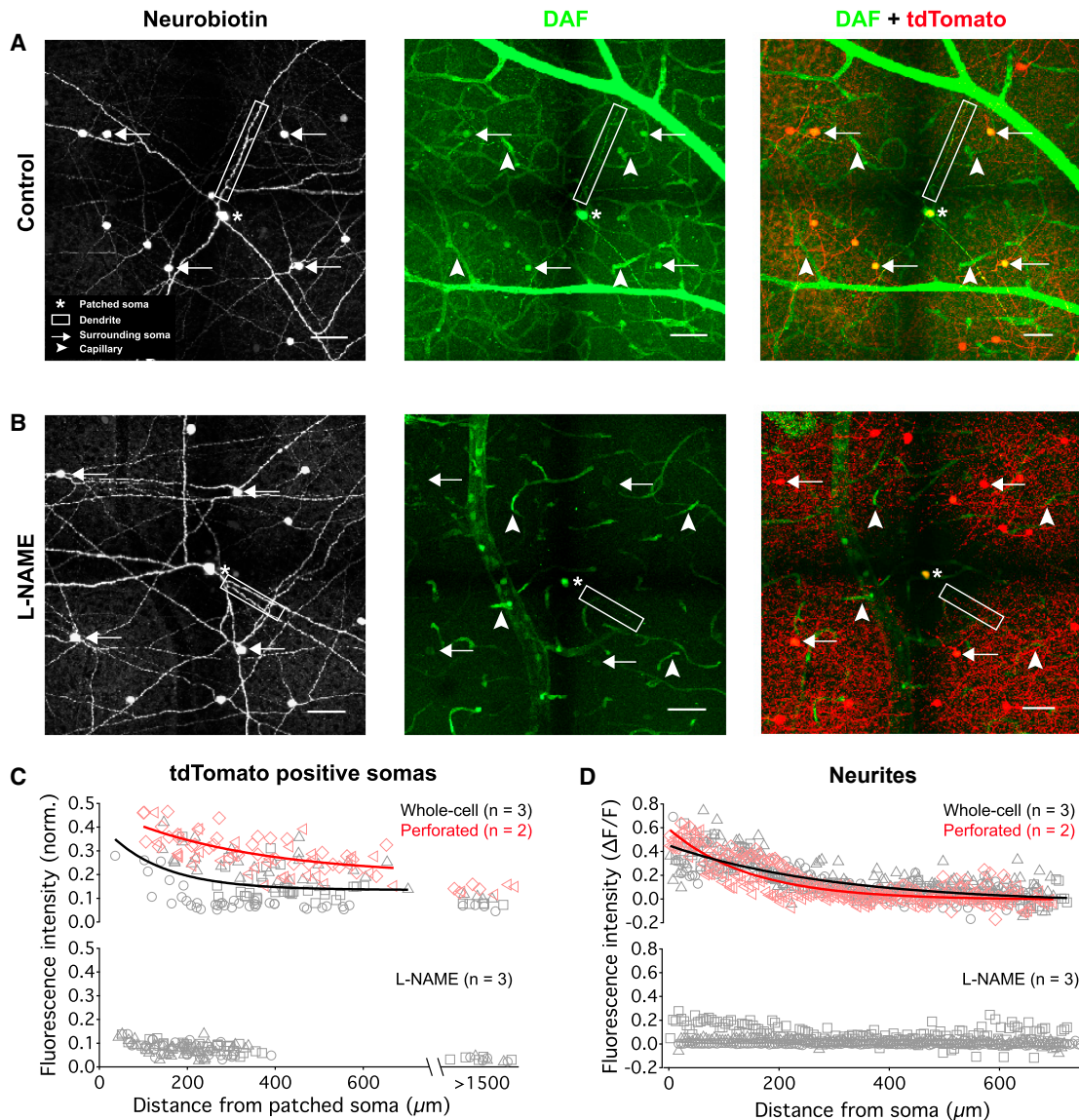


### Figure 5. Depolarizing Individual nNOS-2 ACs Produces NO in the IPL

(A) From left to right: neurobiotin fill of an example nNOS-2 AC, DAF fluorescence measured after depolarizing a single nNOS-2 cell in the GCL by +40 mV from resting membrane potential by a train of current injection pulses at 0.5 Hz for 15 min, and merge of the DAF and tdTomato channels. Symbols denote a patched soma (asterisk), neurite (box), surrounding somata (arrow), and capillaries (arrowhead). All images were acquired using confocal microscopy. Scale bars, 50  $\mu\text{m}$ .

(B) The same as in (A) but in the presence of the bath-applied NOS inhibitor L-NAME.

(C) DAF fluorescence intensity in tdTomato-positive somata as a function of distance from the patched soma. Intensities were normalized to the intensity in the patched soma. Different symbols indicate different retinas using whole-cell depolarizations (gray symbols, n = 3) or perforated patch depolarizations (red symbols, n = 2). Solid lines are single exponential fits excluding the patched soma for both whole-cell access depolarization (black) and perforated patch depolarization (red).

(D) DAF fluorescence intensity in the neurites of the patched cell as a function of distance from the soma. Symbols are as in (C) (whole cell, n = 3; perforated patch, n = 2). Exponential fits are the same as in (C).

nNOS-2 AC is a conservative estimate of NO release from this cell. Inhibiting NOS throughout the retina with  $N_{\omega}$ -nitro-L-arginine methyl ester (L-NAME) largely prevented the injected AC from synthesizing NO, and we observed only a weak DAF signal in the injected soma and no signal in its neurites or in other somata (Figures 5B–5D). We observed similarly diminished fluo-

rescence in the blood vessels, consistent with the action of L-NAME as a blocker of both eNOS and nNOS.

Both nNOS-1 and nNOS-2 ACs are immunopositive for nNOS (Figure S1), so we performed the same NO imaging experiments while depolarizing nNOS-1 ACs. We observed minimal DAF signals in the dendrites and axons of nNOS-1 ACs, similar to the

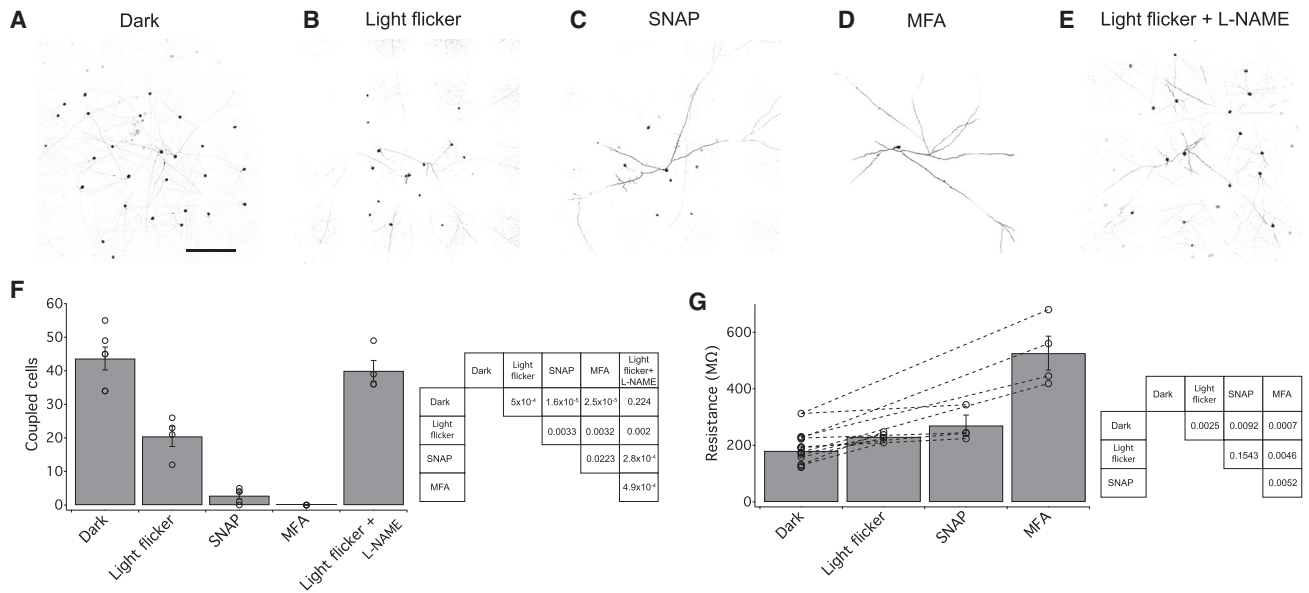


**Figure 6. Gap Junction Network Coupling Is Regulated by Light and NO and Affects Input Resistance**

(A–E) Degree of coupling (denoted by dark somata) derived from a single nNOS-2 AC filled with neurobiotin after exposure to (A) darkness, (B) full-field light flicker, (C) SNAP, (D) MFA, and (E) full-field light flicker in the presence of L-NAME prior to whole-cell access. Scale bars, 200  $\mu$ m.

(F) Population data showing the average number of coupled cells for each condition (dark versus light,  $p < 10^{-3}$ ; dark versus SNAP,  $p < 10^{-4}$ ; dark versus MFA,  $p < 10^{-4}$ ; paired t tests; dark versus L-NAME,  $p > 0.23$ ;  $n = 4$  for each comparison). A table of p values for t tests is shown to the right of the graph.

(G) Resistance measurements from individual nNOS-2 ACs in darkness followed by exposure to light flicker, SNAP, MFA, or light flicker in the presence of L-NAME. Statistical significance between resistance in the dark and other conditions: dark versus light flicker,  $p < 10^{-2}$ ; dark versus SNAP,  $p < 10^{-2}$ ; dark versus MFA,  $p < 10^{-3}$ ; dark versus light flicker + L-NAME,  $p > 0.23$  (paired Student's t tests,  $n = 4$  for each comparison). A table of p values for t tests is shown to the right of the graph.

L-NAME condition in nNOS-2 ACs (Figure S4), suggesting that nNOS-2 ACs are the main NO source of the inner retina.

To relate the NO release driven by nNOS-2 ACs back to their light responses, we replicated previous results on flicker-induced increases in NO. We found that NO levels increased dramatically in the IPL with flickering light in the photopic regime but not with constant illumination at the same mean level (Figure S5). As a positive control to verify that DAF detects NO, we applied the exogenous NO donor S-nitroso-N-acetylpenicillamine (SNAP). The peak location of NO release in the IPL with light flicker was consistent with the location of nNOS-2 AC neurites.

### nNOS-2 AC Coupling Is Regulated by Light and NO

A molecular pathway connecting NO to gap junction conductance has been identified previously. The NO receptor soluble guanylyl cyclase (sGC) catalyzes formation of the effector molecule cyclic guanosine monophosphate (cGMP). The cGMP-dependent protein kinase (PKG) then phosphorylates Cx45 gap junctions, reducing their conductance (Lu and McMahon, 1997). We confirmed that nNOS-2 ACs contain sGC (Figure S6), so we next asked whether NO could modulate the nNOS-2 AC gap junction network, perhaps through this same molecular pathway (Figure 6).

We first tested the luminance dependence of nNOS-2 AC coupling using a bright, full-field flicker stimulus. Light flicker reduced the coupled network from  $44 \pm 3$  to  $21 \pm 3$  cells (Figures 6A and 6B;  $n = 6$  dark,  $n = 4$  networks). To determine whether

coupling depends on NO, we applied SNAP, which reduced tracer coupling to  $3 \pm 1$  cells (Figure 6C;  $n = 5$ ). Application of the gap junction blocker MFA eliminated all coupling, leaving only an isolated cell filled with neurobiotin (Figure 6D;  $n = 4$ ). To confirm that the flicker-induced decoupling of nNOS-2 ACs relied on NO synthesis, we inhibited NOS with L-NAME and repeated the flicker experiments. In the presence of L-NAME, light flicker was unable to decouple the network, and we measured a similar number of coupled cells as in the dark (Figure 6E;  $n = 6$  dark,  $n = 4$  L-NAME).

To study how the changes we observed in anatomical coupling might affect the electrical properties of the network, we measured the input resistance of nNOS-2 ACs across the same set of conditions in which we measured tracer coupling. Decreases in coupling should correspond to reduced gap junction conductance throughout the network, increasing input resistance (Figure 6G). In the dark, the input resistance of a single cell was  $180 \pm 14$  megaohms (M $\Omega$ ) ( $n = 17$  cells). In accordance with our tracer coupling results, the resistance increased to  $230 \pm 8$  M $\Omega$  ( $n = 4$ ) after light flicker. Separately, perfusion of SNAP over the tissue increased the resistance to  $270 \pm 37$  M $\Omega$  ( $n = 4$ ). Finally, we obtained the resistance of individual nNOS-2 ACs ( $526 \pm 60$  M $\Omega$ ,  $n = 4$ ) isolated from the network via complete block of gap junctions in MFA. Each resistance measurement was significantly different from the value in darkness (Figure 6G, right). We interpret the magnitude of the input resistance changes in the context of a model of the network below.

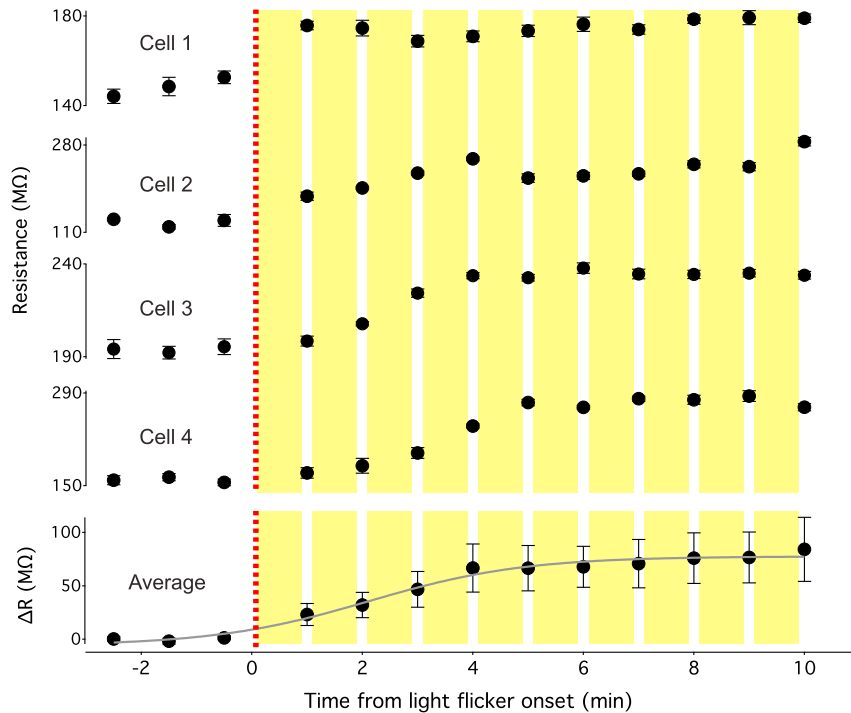


**Figure 7. Kinetics of Light Flicker-Induced Resistance Changes in the nNOS Network**

Input resistance measurements of nNOS cells ( $n = 4$ ) and their population average starting from darkness (baseline), followed by a light flicker stimulus presented at 1-min intervals. The gray line shows sigmoid fit to population data.

We also measured the kinetics of input resistance changes induced by light flicker (Figure 7). In four cells, we made baseline resistance measurements in darkness and then re-measured at 1-min intervals following the same light flicker stimulus described previously. Input resistance increased rapidly in all 4 cells. The average resistance increase was well fit by a sigmoid with an amplitude of 84 M $\Omega$  and a half-maximal timescale of 2.1 min.

### Modeling the Effect of Gap Junction Modulation on the nNOS-2 AC Network

Having established that electrical coupling in the nNOS-2 AC network is modulated by light through NO, we wanted to explore the biophysical properties of the neurons and their gap junctions that could account for our recorded data. We used a cable model in the NEURON simulation environment (Hines and Carnevale, 1997) to link our anatomical and physiological measurements of the nNOS-2 AC network. We modeled a network of 36 gap junction-coupled nNOS-2 ACs (Figure 8A; Figures S7A–S7D). The densities of somata, neurites, and gap junctions in the model were taken from our anatomical measurements (Table S1), and both individual cell and network parameters of model construction were tested for robustness across wide ranges of values (Figures S7E–S7L). Details of the model construction are given in the STAR Methods, and all parameters are listed in Table S1.

A key unknown from our experiments was the conductance of each gap junction connection. We varied the gap junction conductance in the model to study its effect on two measured properties, input resistance and coupling coefficient, both modeled with somatic current injections to match our experiments. Input resistance was tightly linked to gap junction conductance with little variation across 10 different instantia-

tions of the network (Figure 8D; SD in the shaded region). Because of the steep nonlinearity of this relationship, the modest 23% increase in input resistance we observed between dark and light flicker conditions corresponds to a 55% reduction in gap junction conductance, from 4.4 nS to 2.0 nS.

With the gap junction conductance fixed at 4.4 nS to match the input resistance we measured in the dark, we modeled the coupling coefficient from a single central cell (#21 in Figure 8A) to each other cell in the network. Although the coupling coefficients in the model were consistent with our measurements, they were highly variable based on the number and location of connections between the two cells. The shallow dependence of the coupling coefficient on the distance between somata in the network matched our paired whole-cell measurements (Figure 8C). One reason for this discrepancy in variance could be that we targeted pairs for recording based on the transmission of Alexa Fluor 488; this likely biased us toward highly coupled cells. Additionally, it is possible that the real nNOS-2 AC network constrains this variability by creating a more uniform distribution of the number of gap junctions between each pair of cells than we modeled here. Future experiments with large-scale imaging and physiology might be able to resolve such questions about network heterogeneity.

### DISCUSSION

Neuromodulators are rarely viewed through the same lens as conventional neurotransmitters, but several decades of research have revealed a diverse and critical role for these compounds in neural signaling pathways throughout the CNS. One of the most pervasive and impactful neuromodulators is the freely diffusible gas NO (Garthwaite, 2008). NO has long been known to influence neural processing and neurovascular coupling in the retina and in the brain, but a physiological link to NO release in the retina had not been identified. Several possible AC sources of NO have been characterized predominantly through morphology and nNOS immunoreactivity in the retinas of rats (Lee et al., 2003; Pang et al., 2010), rabbits (Koistinaho et al., 1993), and cats (Kim et al., 1999; Kim et al., 2000). Using the nNOS-Cre transgenic line, we discovered that nNOS-2 ACs are embedded in a vast homologous gap junction network (Figures 1 and 2). We reported the first physiological recordings of the nNOS-2 AC in the mouse retina (Figure 3), showed that their depolarization leads to

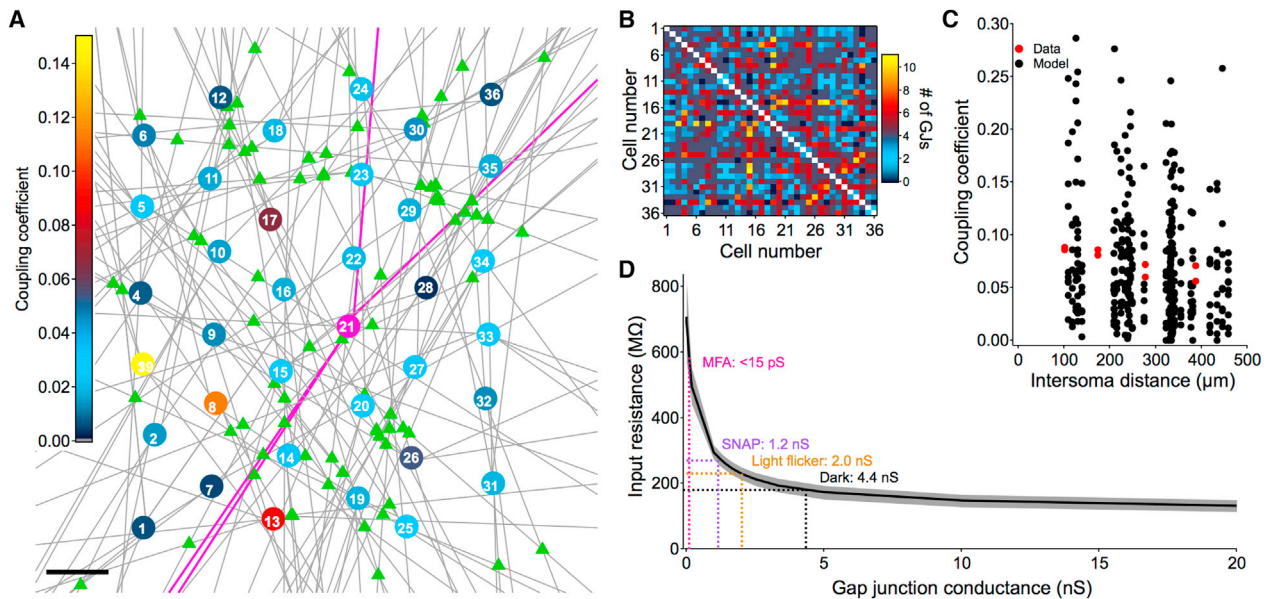


**Figure 8. Biophysical Model of the nNOS-2 AC Network**

(A) Diagram of an instantiation of the network model. Somata are numbered, and their neurites are shown in gray. Cell 21 was injected with current for coupling measurements, and its soma and neurites are colored magenta. All other somata are colored according to their coupling coefficient with cell 21. Locations of gap junctions are shown as green triangles. Scale bar, 100  $\mu\text{m}$ .

(B) Heatmap of the number of gap junctions made between cells in the network shown in (A).

(C) Coupling coefficients of the 35 cell pairs tested in 10 different instantiations of the model as in (A), plotted versus the distance between somata. Data points from Figure 2E are shown in red.

(D) Median input resistance of the 36 model cells as a function of gap junction conductance. The black line is the mean value across 10 instantiations of the model. SD is shown by the shaded region. Dotted lines highlight the 4 different experimentally measured values of input resistance from Figure 6G and the corresponding values of gap junction conductance in the model.

$\text{Ca}^{2+}$  influx (Figure 4), and that depolarization of single cells leads to NO release (Figure 5). We also established that light-dependent NO release decouples the network (Figures 6 and 7), and we constructed a biophysical model using our morphological and physiological measurements that recapitulated some of the key features of our data (Figure 8).

Two factors about our experimental preparation would be predicted to cause us to underestimate the effects of NO. First, the nNOS-Cre line is a knockin-knockout line in which Cre replaces nNOS, so nNOS expression is lower in the heterozygous mice we used than in WT mice. Second, we used a high perfusion rate (10 mL/min) to maintain photoreceptor health, but this high flow likely washed out NO gas much faster than it would diffuse in the intact eye. For these reasons, we would expect even larger NO-dependent changes in nNOS-2 AC coupling *in vivo*.

#### Rapid Kinetics in NOACs May Support Fast NO Release

nNOS-2 ACs are non-spiking interneurons that transiently depolarize in response to both light onset and offset (Figure 3). These response characteristics are similar to those observed in the type 1 NOAC in the rat retina (Pang et al., 2010) and morphologically similar WA-2/3 cells identified in the choline acetyltransferase (ChAT)-EGFP transgenic mouse line (Knop et al., 2014). We also found that, for a fixed contrast, their depolarizations get larger and faster with increases in background luminance (Figures 3B and 3C). Not only do nNOS-2 ACs have transient light re-

sponses, they also have rapidly inactivating  $\text{Ca}^{2+}$  channels (Figures 4E and 4F; Figures S3C and S3D). The combination of these properties makes them well suited to report relatively fast changes in contrast at photopic light levels (Vielma et al., 2012), exactly the stimulus conditions that elicit maximal NO production (Blom et al., 2012; Eldred and Blute, 2005; Koistinaho et al., 1993; Neal et al., 1998). These dynamics sharply contrast with dopaminergic ACs, which have sustained light responses and tonically fire action potentials, keeping their  $\text{Ca}^{2+}$  channels out of the inactivated state (Puopolo et al., 2001).

Why does the retina have these two neuromodulatory systems with different kinetics, both involved in light adaptation? One possibility is that, although dopamine controls gain on the circadian timescale, NO facilitates transitions to photopic circuits based on more rapid changes in light intensity. A gradual decrease in gain at dawn may rely on dopamine, but regaining sensitivity when an animal emerges from a dark shelter during the day may, instead, rely on NO. Indeed, we observed changes in input resistance (because of decoupling) in the nNOS-2 AC network over several minutes following the onset of light flicker (Figure 7).

Evidence that NO is involved in engaging photopic circuits comes from studies of its effects in both the outer and the inner retina. In the outer retina, NO increases the responses of ON cone bipolar cells to weak stimuli by modulating metabotropic glutamate receptors expressed on their dendrites (Snellman

and Nawy, 2004). In the inner retina, one of the first targets of NO signaling to be identified was the Cx45 side of the Cx36-Cx45 hetero-junctions between All ACs and ON cone bipolar cells (Mills and Massey, 1995). NO decreases the conductance of these gap junctions, reducing the influence of the scotopic rod bipolar pathway through Alls on the photopic cone bipolar pathway. More recently, NO has been shown to modulate the temporal properties of the glutamate response of OFF bipolar cells through a retrograde signaling pathway from NOACs onto type 4 OFF bipolar cell terminals (Vielma et al., 2014). Another study revealed that a novel, NO-dependent S-nitrosylation mechanism lowered the threshold of bipolar cell  $\text{Ca}^{2+}$  currents, enhancing glutamate output (Tooker et al., 2013).

NO also has a well-characterized role as a vasodilator throughout the body (Förstermann and Sessa, 2012; Jeffrey Man et al., 2014; Toda and Okamura, 2011). The retinal circulation consists of three layers of capillaries (Chan et al., 2012). Vessels connecting the superficial and middle capillary networks pass through the IPL, where NO release could regulate their diameter to control the balance of blood flow between these two layers. *In vivo* experiments in rats have shown that flickering light causes a transient decrease in flow in the superficial capillary network and a sustained increase in flow in the middle capillary network (Kornfield and Newman, 2014). The molecular pathway by which NO modulates vessel diameter in the retina (where it sometimes causes constriction instead of dilation) may differ from that in the brain (Metea and Newman, 2006), and it may even differ between capillary layers (Biesecker et al., 2016). Understanding the role of NO in retinal circulation and its dysregulation in disease will depend on a better understanding of the relationship between visual stimuli and NO release.

Our study places these findings on the effects of NO in the context of the key AC responsible for synthesizing this modulator in the inner retina. Extensive coupling in the nNOS-2 AC network may promote homogeneous, lateral spread of NO within a specific layer in the middle of the IPL. We observed a more widespread NO signal with light flicker (Figure S5A), but the interpretation of this result is complicated by the unipolar nature of DAF; it reports an accumulated NO signal following diffusion.

### Gap Junction Modulation to Control Excitability through Input Resistance

Gap junctions serve a variety of functional roles throughout the CNS. Perhaps the most extensive work on gap junctions has been in the vertebrate retina, where electrical coupling has been demonstrated in each of the five major classes of neurons (Völgyi et al., 2009). Here we suggest yet another role for gap junctions in the retina, as a mechanism for modulating the electrical resistance of a coupled network to alter excitability.

A surprising experimental finding of our study was that changes in coupling in the nNOS-2 AC network mediated by light-dependent NO release can substantially alter the input resistance of the cells (Figure 6G). Our model predicted that the change in input resistance we measured following light flicker represented a 55% reduction in gap junction conductance. Light-dependent changes in coupling have been shown to alter the electrical properties of the horizontal cell network in the outer

retina (Benda et al., 2001; Kamermans et al., 1996). How does decoupling in the nNOS-2 AC network affect signal flow and, ultimately, NO release?

Unlike our somatic current injections, realistic light stimuli would activate segments of many nNOS-2 ACs simultaneously where they receive inputs from bipolar cells, as confirmed by the presence of excitatory synapses (Figure S6). We simulated input from spots of light at various positions in the network, and we measured the resulting spread of voltage (Figure S8). As expected, the voltage response was maximal near the input location and decayed along both stimulated and coupled neurites. Reducing the gap junction conductance to 2.0 nS, the value we measured after flickering light, had opposite effects depending on network location. Distal to the stimulus, voltage spread was attenuated because less current flowed through gap junctions. Proximal to the stimulus, however, the maximum voltage response increased. Reducing current flow in the distal network effectively increased current density in the proximal network, leading to a larger depolarization (Figure 8E, right). Across 100 different stimulus locations, the maximum voltage was always larger in model networks with gap junctions set to 2.0 nS than in those with this parameter set to 4.4 nS (Figure S8B). One can think of the gap junctions in their most open state in the dark as providing a “current sink” to distribute synaptic currents broadly throughout the network, limiting their ability to depolarize individual neurites. Following light flicker, when their conductance is reduced, the current sink is less effective. To explore possible effects of this resistance change on calcium influx, we used our measurements of the relationship between voltage and  $\text{Ca}^{2+}$  current (Figure 4G). The dependence of  $\text{Ca}^{2+}$  on voltage served to amplify the effect of reducing gap junction conductance. Calcium influx was up to 30% higher in the decoupled network state at the location of peak depolarization in the example network (Figures S8C and S8D).

### Biophysical Specializations in the nNOS-2 AC Network

The fact that Alexa Fluor 488 traveled through the nNOS-2 AC gap junctions (Figure 1C) indicated that they were somehow different than most other gap junctions in the retina, and the estimate of 4.4 nS conductance in the dark from our model made this point directly. Gap junctions between RGCs have been estimated to be in the range of  $\sim 1$  nS (Trenholm et al., 2013). Gap junctions between photoreceptors are  $\sim 500$  pS in their most open state (Jin and Ribelayga, 2016). Even the gap junctions between All ACs, the canonical electrical network of the inner retina, are  $\sim 700$  pS (Veruki and Hartveit, 2002). Only the Cx57 gap junctions between horizontal cells have been reported to have a similarly large conductance (DeVries and Schwartz, 1989; Lasater, 1987; Lasater and Dowling, 1985). The massive conductance of the nNOS-2 AC gap junctions is an essential feature because it allows a change in conductance to create a substantial change in input resistance (Figure 8D).

The morphology of nNOS-2 ACs also contributes to their functional niche. The long, unbranching processes of wide-field ACs are generally thought to propagate signals quickly across large regions of the retina using action potentials (Masland, 2012). nNOS-2 ACs, however, do not fire action potentials (Figure 3D), so why do they have such long neurites? First, even without

active propagation, the passive properties of nNOS-2 ACs are tuned for long spatial scales (Manookin et al., 2015). Our paired recordings found high coupling coefficients for somata nearly 400  $\mu\text{m}$  apart (Figure 2), which means the path length of neurites connecting these cells was even longer. Our model recapitulated the long electrotonic length constant of the nNOS-2 AC neurites ( $\sim 1.7$  mm) because of their large diameter and their high membrane resistivity (Table S1). Another functional constraint on the morphology of nNOS-2 ACs may be dense connectivity to distant cells. By sending long, unbranching neurites at apparently random angles relative to each other, nNOS-2 ACs come into direct contact with many more cells (Figure 8B) than would be possible in a more traditional network of nearest neighbors, like that of the All ACs (Veruki and Hartveit, 2002). nNOS-2 thus joins a list of wide-field non-spiking ACs in which specialized morphology subserves a particular task (Grimes, 2012), including the A17 AC, which is specialized for compartmentalized feedback synapses (Grimes et al., 2010), and the wiry AC in primates, which may serve a role in motion processing (Manookin et al., 2015).

nNOS-2 ACs also contain gamma-aminobutyric acid (GABA) (Zhu et al., 2014), and possible targets of these cells for direct inhibition, their modulation with light, and the roles of co-release of GABA and NO will all be subjects of future studies.

## STAR★METHODS

Detailed methods are provided in the online version of this paper and include the following:

- KEY RESOURCES TABLE
- CONTACT FOR REAGENT AND RESOURCE SHARING
- EXPERIMENTAL MODEL AND SUBJECT DETAILS
- METHOD DETAILS
  - Electrophysiology
  - Paired recordings
  - Visual stimuli
  - Calcium imaging
  - DAF imaging
  - Tracer coupling
  - Immunohistochemistry
  - Biophysical network model
- QUANTIFICATION AND STATISTICAL ANALYSIS
  - Statistical analysis
  - Physiology analysis
  - Image analysis
- DATA AND SOFTWARE AVAILABILITY

## SUPPLEMENTAL INFORMATION

Supplemental Information includes eight figures and one table and can be found with this article online at <https://doi.org/10.1016/j.neuron.2018.09.047>.

## ACKNOWLEDGMENTS

We thank our lab manager, Susan Wohlgenant, for her never-ending assistance with experimental preparation, antibody staining, and oversight of our mouse colonies and breeding. We also thank Steve DeVries and Yongling Zhu for providing the original mice used to make the preliminary findings on

this project and for supplemental mice throughout the project and Petri Ala-Laurila, Fred Rieke, Mike Manookin, Will Grimes, Tiffany Schmidt, and Felice Dunn for their comments on early drafts of the manuscript. This research project was funded by Ruth L. Kirschstein National Research Service Award (NRSA) postdoctoral fellowship 1F32EY025930-01, NIH DP2-DEY026770A and T32GM008152, and the Research to Prevent Blindness Career Development Award.

## AUTHOR CONTRIBUTIONS

J.J., A.N., and G.W.S. designed the experiments, wrote the paper, and prepared the figures. Z.F.J. and G.W.S. created the computational model, prepared the modeling figures, and helped to write the manuscript.

## DECLARATION OF INTERESTS

The authors declare no competing interests.

Received: November 6, 2017

Revised: March 28, 2018

Accepted: September 25, 2018

Published: October 25, 2018

## REFERENCES

- Badea, T.C., and Nathans, J. (2004). Quantitative analysis of neuronal morphologies in the mouse retina visualized by using a genetically directed reporter. *J. Comp. Neurol.* *480*, 331–351.
- Benda, J., Bock, R., Rujan, P., and Ammermüller, J. (2001). Asymmetrical dynamics of voltage spread in retinal horizontal cell networks. *Vis. Neurosci.* *18*, 835–848.
- Berntson, A., and Taylor, W.R. (2000). Response characteristics and receptive field widths of on-bipolar cells in the mouse retina. *J. Physiol.* *524*, 879–889.
- Berson, D.M., Dunn, F.A., and Takao, M. (2002). Phototransduction by retinal ganglion cells that set the circadian clock. *Science* *295*, 1070–1073.
- Biesecker, K.R., Srienc, A.I., Shimoda, A.M., Agarwal, A., Bergles, D.E., Kofuji, P., and Newman, E.A. (2016). Glial Cell Calcium Signaling Mediates Capillary Regulation of Blood Flow in the Retina. *J. Neurosci.* *36*, 9435–9445.
- Blom, J., Giove, T., Deshpande, M., and Eldred, W.D. (2012). Characterization of nitric oxide signaling pathways in the mouse retina. *J. Comp. Neurol.* *520*, 4204–4217.
- Chan, G., Balaratnasingam, C., Yu, P.K., Morgan, W.H., McAllister, I.L., Cringle, S.J., and Yu, D.-Y. (2012). Quantitative morphometry of perfoveal capillary networks in the human retina. *Invest. Ophthalmol. Vis. Sci.* *53*, 5502–5514.
- DeVries, S.H., and Schwartz, E.A. (1989). Modulation of an electrical synapse between solitary pairs of catfish horizontal cells by dopamine and second messengers. *J. Physiol.* *414*, 351–375.
- Eldred, W.D., and Blute, T.A. (2005). Imaging of nitric oxide in the retina. *Vision Res.* *45*, 3469–3486.
- Famiglietti, E.V. (1992). Polyaxonal amacrine cells of rabbit retina: morphology and stratification of PA1 cells. *J. Comp. Neurol.* *316*, 391–405.
- Förstermann, U., and Sessa, W.C. (2012). Nitric oxide synthases: regulation and function. *Eur. Heart J.* *33*, 829–837.
- Garthwaite, J. (2008). Concepts of neural nitric oxide-mediated transmission. *Eur. J. Neurosci.* *27*, 2783–2802.
- Garthwaite, J., Charles, S.L., and Chess-Williams, R. (1988). Endothelium-derived relaxing factor release on activation of NMDA receptors suggests role as intercellular messenger in the brain. *Nature* *336*, 385–388.
- Grimes, W.N. (2012). Amacrine cell-mediated input to bipolar cells: variations on a common mechanistic theme. *Vis. Neurosci.* *29*, 41–49.
- Grimes, W.N., Zhang, J., Graydon, C.W., Kachar, B., and Diamond, J.S. (2010). Retinal parallel processors: more than 100 independent microcircuits operate within a single interneuron. *Neuron* *65*, 873–885.

- Hattar, S., Lucas, R.J., Mrosovsky, N., Thompson, S., Douglas, R.H., Hankins, M.W., Lem, J., Biel, M., Hofmann, F., Foster, R.G., and Yau, K.W. (2003). Melanopsin and rod-cone photoreceptive systems account for all major accessory visual functions in mice. *Nature* 424, 76–81.
- Hines, M.L., and Carnevale, N.T. (1997). The NEURON simulation environment. *Neural Comput.* 9, 1179–1209.
- Jacoby, J., and Schwartz, G.W. (2017). Three Small-Receptive-Field Ganglion Cells in the Mouse Retina Are Distinctly Tuned to Size, Speed, and Object Motion. *J. Neurosci.* 37, 610–625.
- Jacoby, J., Zhu, Y., DeVries, S.H., and Schwartz, G.W. (2015). An Amacrine Cell Circuit for Signaling Steady Illumination in the Retina. *Cell Rep.* 13, 2663–2670.
- Jakobs, T.C., Koizumi, A., and Masland, R.H. (2008). The spatial distribution of glutamatergic inputs to dendrites of retinal ganglion cells. *J. Comp. Neurol.* 510, 221–236.
- Jeffrey Man, H.S., Tsui, A.K.Y., and Marsden, P.A. (2014). Nitric oxide and hypoxia signaling. *Vitam. Horm.* 96, 161–192.
- Jin, N.G., and Ribelayga, C.P. (2016). Direct Evidence for Daily Plasticity of Electrical Coupling between Rod Photoreceptors in the Mammalian Retina. *J. Neurosci.* 36, 178–184.
- Kamermans, M., Haak, J., Habraken, J.B., and Spekrijse, H. (1996). The size of the horizontal cell receptive fields adapts to the stimulus in the light adapted goldfish retina. *Vision Res.* 36, 4105–4119.
- Kim, I.B., Lee, E.J., Kim, K.Y., Ju, W.K., Oh, S.J., Joo, C.K., and Chun, M.H. (1999). Immunocytochemical localization of nitric oxide synthase in the mammalian retina. *Neurosci. Lett.* 267, 193–196.
- Kim, K.Y., Ju, W.K., Oh, S.J., and Chun, M.H. (2000). The immunocytochemical localization of neuronal nitric oxide synthase in the developing rat retina. *Exp. Brain Res.* 133, 419–424.
- Knop, G.C., Pottek, M., Monyer, H., Weiler, R., and Dedek, K. (2014). Morphological and physiological properties of enhanced green fluorescent protein (EGFP)-expressing wide-field amacrine cells in the ChAT-EGFP mouse line. *Eur. J. Neurosci.* 39, 800–810.
- Koistinaho, J., Swanson, R.A., de Vente, J., and Sagar, S.M. (1993). NADPH-diaphorase (nitric oxide synthase)-reactive amacrine cells of rabbit retina: putative target cells and stimulation by light. *Neuroscience* 57, 587–597.
- Kojima, H., Urano, Y., Kikuchi, K., Higuchi, T., Hirata, Y., and Nagano, T. (1999). Fluorescent Indicators for Imaging Nitric Oxide Production. *Angew. Chem. Int. Ed. Engl.* 38, 3209–3212.
- Kornfield, T.E., and Newman, E.A. (2014). Regulation of blood flow in the retinal trilateral vascular network. *J. Neurosci.* 34, 11504–11513.
- Lasater, E.M. (1987). Retinal horizontal cell gap junctional conductance is modulated by dopamine through a cyclic AMP-dependent protein kinase. *Proc. Natl. Acad. Sci. USA* 84, 7319–7323.
- Lasater, E.M., and Dowling, J.E. (1985). Dopamine decreases conductance of the electrical junctions between cultured retinal horizontal cells. *Proc. Natl. Acad. Sci. USA* 82, 3025–3029.
- Lee, E.-J., Kim, K.-Y., Gu, T.-H., Moon, J.-I., Kim, I.-B., Lee, M.-Y., Oh, S.-J., and Chun, M.-H. (2003). Neuronal nitric oxide synthase is expressed in the axotomized ganglion cells of the rat retina. *Brain Res.* 986, 174–180.
- Lu, C., and McMahon, D.G. (1997). Modulation of hybrid bass retinal gap junctional channel gating by nitric oxide. *J. Physiol.* 499, 689–699.
- Manookin, M.B., Puller, C., Rieke, F., Neitz, J., and Neitz, M. (2015). Distinctive receptive field and physiological properties of a wide-field amacrine cell in the macaque monkey retina. *J. Neurophysiol.* 114, 1606–1616.
- Masland, R.H. (2012). The tasks of amacrine cells. *Vis. Neurosci.* 29, 3–9.
- McMurry, J.L., Chrestensen, C.A., Scott, I.M., Lee, E.W., Rahn, A.M., Johansen, A.M., Forsberg, B.J., Harris, K.D., and Salerno, J.C. (2011). Rate, affinity and calcium dependence of nitric oxide synthase isoform binding to the primary physiological regulator calmodulin. *FEBS J.* 278, 4943–4954.
- Metea, M.R., and Newman, E.A. (2006). Glial cells dilate and constrict blood vessels: a mechanism of neurovascular coupling. *J. Neurosci.* 26, 2862–2870.
- Mills, S.L., and Massey, S.C. (1995). Differential properties of two gap junctional pathways made by All amacrine cells. *Nature* 377, 734–737.
- Neal, M., Cunningham, J., and Matthews, K. (1998). Selective release of nitric oxide from retinal amacrine and bipolar cells. *Invest. Ophthalmol. Vis. Sci.* 39, 850–853.
- Nir, I., Haque, R., and Iuvone, P.M. (2000). Diurnal metabolism of dopamine in the mouse retina. *Brain Res.* 870, 118–125.
- Olteidal, L., Veruki, M.L., and Hartveit, E. (2009). Passive membrane properties and electrotonic signal processing in retinal rod bipolar cells. *J. Physiol.* 587, 829–849.
- Pang, J.-J., Gao, F., and Wu, S.M. (2010). Light responses and morphology of bNOS-immunoreactive neurons in the mouse retina. *J. Comp. Neurol.* 518, 2456–2474.
- Park, S.J.H., Borghuis, B.G., Rahmani, P., Zeng, Q., Kim, I.-J., and Demb, J.B. (2015). Function and Circuitry of VIP+ Interneurons in the Mouse Retina. *J. Neurosci.* 35, 10685–10700.
- Puopolo, M., Hochstetler, S.E., Gustincich, S., Wightman, R.M., and Raviola, E. (2001). Extrasynaptic release of dopamine in a retinal neuron: activity dependence and transmitter modulation. *Neuron* 30, 211–225.
- Raman, I.M., and Bean, B.P. (1999). Ionic currents underlying spontaneous action potentials in isolated cerebellar Purkinje neurons. *J. Neurosci.* 19, 1663–1674.
- Rempe, M.J., Spruston, N., Kath, W.L., and Chopp, D.L. (2008). Compartmental neural simulations with spatial adaptivity. *J. Comput. Neurosci.* 25, 465–480.
- Schwartz, G.W., Okawa, H., Dunn, F.A., Morgan, J.L., Kerschensteiner, D., Wong, R.O., and Rieke, F. (2012). The spatial structure of a nonlinear receptive field. *Nat. Neurosci.* 15, 1572–1580.
- Snellman, J., and Nawy, S. (2004). cGMP-dependent kinase regulates response sensitivity of the mouse on bipolar cell. *J. Neurosci.* 24, 6621–6628.
- Stafford, D.K., and Dacey, D.M. (1997). Physiology of the A1 amacrine: a spiking, axon-bearing interneuron of the macaque monkey retina. *Vis. Neurosci.* 14, 507–522.
- Surprenant, A., Shen, K.Z., North, R.A., and Tatsumi, H. (1990). Inhibition of calcium currents by noradrenaline, somatostatin and opioids in guinea-pig submucosal neurones. *J. Physiol.* 431, 585–608.
- Tien, N.-W., Kim, T., and Kerschensteiner, D. (2016). Target-Specific Glycinergic Transmission from VGluT3-Expressing Amacrine Cells Shapes Suppressive Contrast Responses in the Retina. *Cell Rep.* 15, 1369–1375.
- Toda, N., and Okamura, T. (2011). Modulation of renal blood flow and vascular tone by neuronal nitric oxide synthase-derived nitric oxide. *J. Vasc. Res.* 48, 1–10.
- Tooker, R.E., Lipin, M.Y., Leuranguer, V., Rozsa, E., Bramley, J.R., Harding, J.L., Reynolds, M.M., and Vigh, J. (2013). Nitric oxide mediates activity-dependent plasticity of retinal bipolar cell output via S-nitrosylation. *J. Neurosci.* 33, 19176–19193.
- Trenholm, S., McLaughlin, A.J., Schwab, D.J., and Awatramani, G.B. (2013). Dynamic tuning of electrical and chemical synaptic transmission in a network of motion coding retinal neurons. *J. Neurosci.* 33, 14927–14938.
- Tricoire, L., and Vitalis, T. (2012). Neuronal nitric oxide synthase expressing neurons: a journey from birth to neuronal circuits. *Front. Neural Circuits* 6, 82.
- Veruki, M.L., and Hartveit, E. (2002). All (Rod) amacrine cells form a network of electrically coupled interneurons in the mammalian retina. *Neuron* 33, 935–946.
- Vielma, A., Delgado, L., Elgueta, C., Osorio, R., Palacios, A.G., and Schmachtenberg, O. (2010). Nitric oxide amplifies the rat electroretinogram. *Exp. Eye Res.* 91, 700–709.
- Vielma, A.H., Retamal, M.A., and Schmachtenberg, O. (2012). Nitric oxide signaling in the retina: what have we learned in two decades? *Brain Res.* 1430, 112–125.

- Vielma, A.H., Agurto, A., Valdés, J., Palacios, A.G., and Schmachtenberg, O. (2014). Nitric oxide modulates the temporal properties of the glutamate response in type 4 OFF bipolar cells. *PLoS ONE* 9, e114330.
- Völgyi, B., Chheda, S., and Bloomfield, S.A. (2009). Tracer coupling patterns of the ganglion cell subtypes in the mouse retina. *J. Comp. Neurol.* 512, 664–687.
- Wang, G.-Y., van der List, D.A., Nemargut, J.P., Coombs, J.L., and Chalupa, L.M. (2007). The sensitivity of light-evoked responses of retinal ganglion cells is decreased in nitric oxide synthase gene knockout mice. *J. Vis.* 7, 7.1–13.
- Wässle, H., Puller, C., Müller, F., and Haverkamp, S. (2009). Cone contacts, mosaics, and territories of bipolar cells in the mouse retina. *J. Neurosci.* 29, 106–117.
- Zhang, D.-Q., Zhou, T.-R., and McMahon, D.G. (2007). Functional heterogeneity of retinal dopaminergic neurons underlying their multiple roles in vision. *J. Neurosci.* 27, 692–699.
- Zhu, Y., Xu, J., Hauswirth, W.W., and DeVries, S.H. (2014). Genetically targeted binary labeling of retinal neurons. *J. Neurosci.* 34, 7845–7861.

## STAR★METHODS

## KEY RESOURCES TABLE

REAGENT or RESOURCE	SOURCE	IDENTIFIER
<b>Antibodies</b>		
Rabbit polyclonal anti-nNOS	ThermoFisher	Cat# 61-7000; RRID: AB_2313734
Mouse monoclonal anti-sGC $\beta$ -1	Santa Cruz	sc-514183
Rabbit monoclonal anti-PSD-95	Cell Signaling	D27E11
Goat polyclonal anti-ChAT	Millipore	AB144P
Mouse monoclonal anti-Connexin 45	ThermoFisher	Cat# 41-5800; RRID: AB_2533511
Rabbit polyclonal anti-Connexin 36	ThermoFisher	Cat# 51-6200; RRID: AB_2533912
Donkey polyclonal anti-rabbit Alexa Fluor 647	Jackson ImmunoResearch	711-605-152
Donkey anti-mouse Alexa Fluor 647	Life Technologies	A-31571
Streptavidin Dylight 488 conjugate	Thermo Scientific	21832
<b>Experimental Models: Organisms/Strains</b>		
Mouse/nNOS-CreER	Jackson Laboratory	JAX 014541
<b>Chemicals, Peptides, and Recombinant Proteins</b>		
Ames	US Biological Life Sciences	A-1372-25
DAF-FM diacetate	Invitrogen	D23842
SNAP	Sigma-Aldrich	N3398
Neurobiotin	Vector Labs	SP-1150
Vectashield Antifade mounting medium	Vector Labs	H-1000
Alexa Fluor 488	Life Technologies	A10436
Oregon Green BAPTA-1	Life Technologies	O-6806
DNQX	Tocris	0189/10
L-AP4	Tocris	0103
D-AP5	Tocris	0106/1
Cobalt(II) Chloride hexahydrate	Sigma-Aldrich	255599
L-NAME	Sigma-Aldrich	N5751
MFA	Sigma-Aldrich	M4531
Amphotericin	Sigma-Aldrich	A9528
<b>Software and Algorithms</b>		
MATLAB	Mathworks	<a href="https://ch.mathworks.com/products/matlab.html">https://ch.mathworks.com/products/matlab.html</a>
Igor Pro	Wavemetrics	<a href="https://www.wavemetrics.com/">https://www.wavemetrics.com/</a>
Symphony	Symphony consortium	<a href="https://github.com/SchwartzNU/SymphonyAnalysis">https://github.com/SchwartzNU/SymphonyAnalysis</a> <a href="https://github.com/symphony-das">https://github.com/symphony-das</a>
ImageJ/Fiji	NIH	<a href="https://imagej.net/Fiji">https://imagej.net/Fiji</a>
SciScan	Scientifica	<a href="https://www.scientifica.uk.com/products/scientifica-sciscan">https://www.scientifica.uk.com/products/scientifica-sciscan</a>
NEURON	Yale	<a href="https://www.neuron.yale.edu/neuron/download">https://www.neuron.yale.edu/neuron/download</a>
<b>Other</b>		
Two photon laser	Spectra Physics	Mai Tai HP-5085
Confocal microscope	Nikon	A1R
Electrophysiology rig scope	Scientifica	Slicescope Pro 6000
Light Projector	Texas Instruments	DLP LightCrafter 4500

## CONTACT FOR REAGENT AND RESOURCE SHARING

Requests for reagents and resources should be directed to and will be fulfilled by the Lead Contact, Gregory Schwartz ([greg.schwartz@northwestern.edu](mailto:greg.schwartz@northwestern.edu)).

## EXPERIMENTAL MODEL AND SUBJECT DETAILS

All procedures were approved by the Animal Care and Use Committee at Northwestern University. All mice were between 4–10 weeks old and on a mixed B6/129 background. Both male and female mice were used. For all recordings, nNOS-CreER transgenic mice (B6;129S-Nos1<sup>tm1.1(cre/ERT2)Zjh</sup>/J; JAX 014541) were used.

## METHOD DETAILS

### Electrophysiology

nNOS-CreER transgenic mice (B6;129S-Nos1<sup>tm1.1(cre/ERT2)Zjh</sup>/J; JAX 014541) between 4–10 weeks old were dark adapted overnight. All experiments were performed on animals heterozygous for both alleles. Cre was induced with tamoxifen administered in 3 doses (30 mg/Kg) over a period of 5 days starting at P30. Retinae were excised from enucleated whole globes under IR illumination (900 nm) using support from night vision goggles and a dissection scope outfitted with night vision monoculars. All research animals were dispatched in strict accordance with the animal care standards provided by Northwestern University. An intact, whole retina was given 4 relieving cuts and placed flat onto a poly-D-lysine coated glass coverslip and a harp was put over the tissue. The photoreceptors were mounted face down on the coverslip in order to be directly stimulated by visible light from a digital projector focused on the photoreceptor outer segments using the microscope's condenser; this allowed for the recording electrode to easily access the upward-facing ganglion cell layer (GCL) for patching displaced ACs of interest. Retinal explant tissue was superfused with carbogenated Ames solution warmed to 32°C as measured in the bath. Displaced nNOS-2 ACs located in the GCL were targeted using multiphoton laser imaging (980 nm) and identified by their stereotyped morphology as reported by tdTomato fluorescence. Displaced nNOS-2 ACs located in the GCL had a long, single primary neurite (neck) diving into the middle of the inner plexiform layer (IPL); the neck then split into a bifurcation, where two thick secondary neurites projected in opposite directions (Figure 1B). Once patched in current clamp configuration, the identity of the cell could be confirmed by its transient depolarizing response to light stimulus and dye-filled morphology. Most recordings were performed in current clamp with potassium-based intracellular solution; voltage clamp experiments using cesium-based intracellular solution were performed for isolation of calcium currents (Figures 4E–4G). Composition of the internal solutions was as in our previous studies (Jacoby and Schwartz, 2017; Jacoby et al., 2015). Pharmacological reagents were purchased from Tocris Bioscience (DNQX, L-AP4 and D-AP5) and Sigma-Aldrich (SNAP, L-NAME, Cobalt chloride hexahydrate, MFA). Drug concentrations: SNAP, 100 μM; DNQX, 100 μM; L-AP4, 20 μM; D-AP5, 100 μM; L-NAME, 150 μM; CoCl<sub>2</sub>·6H<sub>2</sub>O, 5 mM; MFA, 100 μM).

### Paired recordings

A single nNOS-2 AC was patched in whole cell configuration with intracellular solution containing Alexa Fluor 488. After allowing 15–20 min to fully dialyze and pass through gap junctions to neighboring cells, the two-photon laser (760 nm) was used to detect neighboring, coupled cells in the GCL. The inner limiting membrane (ILM) was gently torn above the now-fluorescent somas of coupled cells, and a paired recording was obtained either by patching (1) the original patched cell and an untouched coupled cell or (2) two new, untouched coupled cells. Each cell in the pair was held in current clamp configuration and injected with 10 current pulses ranging between –200 and +200 pA. Bi-directional current injections were used to stimulate one cell and measure depolarization or hyperpolarization in the other cell and vice-versa.

### Visual stimuli

Visual stimuli were generated with a 912 × 1140 pixel DLP projector (2–3 μm/pixel) at 60 Hz frame rate using a blue LED (450 nm). Light intensities are reported in rod isomerizations (R\*) per rod per second. At this wavelength, M and S cones were stimulated at rates of 0.45 and 0.02 isomerizations, respectively, per rod isomerization. We determined each cell's receptive field (RF) center by locating the optimal spatial response profile in response to bright horizontal and vertical bars across different locations. All stimuli following this centering protocol were adjusted to the position of maximal response to stimulate the cell's RF center. Stimuli presented from different background light levels used 100% positive Weber contrast.

### Calcium imaging

Functional calcium imaging was performed with Oregon Green Bapta-1 (OGB-1; 100 μM). OGB-1 was loaded via patch electrode and given 10 min to fully dialyze before image acquisition, and subsequently excited with a scanning 2-photon laser (Spectra Physics Mai Tai) at 790 nm. Images were acquired with SciScan software (Scientifica) at a framerate of 34.7 Hz, digital zoom factor of 4, and pixel dwell time of 7.2 μs. Depending on the size and shape of the nNOS-2 neurite being imaged during calcium imaging, an image window of either 100 × 32 or 200 × 16 pixels was acquired (5.36 pixels = 1 μM). Current injections (typically 100–250 pA) were delivered via

patch electrode to depolarize the cell to match the physiological response amplitude elicited by light stimuli. All functional imaging experiments were performed in the presence of the synaptic blockers to prevent laser-initiated light responses; AMPA/kainate receptor antagonist DNQX (100  $\mu$ M; Tocris) to block photoreceptor to OFF bipolar cell transmission, metabotropic glutamate receptor agonist L-AP4 (20  $\mu$ M; Tocris) to block photoreceptor to ON bipolar cell transmission, and NMDA receptor antagonist D-AP5 (100  $\mu$ M; Tocris). A similar cocktail was previously shown to block extremely bright channelrhodopsin stimulation of transfected retinal neurons (Park et al., 2015; Tien et al., 2016).

### DAF imaging

The fluorescent NO sensor DAF-FM diacetate was used to determine if changes in NO concentration were taking place within retina exposed to different light conditions (Figure S4) or within the confines of nNOS-2 or nNOS-1 ACs following current injection (Figures 5, S5). Whole retina was bath-loaded by incubating in 10  $\mu$ M DAF for 60 min. This results in the dye being taken up by all cellular tissue, but DAF is essentially non-fluorescent until it reacts with NO, yielding an increase in fluorescence intensity that does not diminish unless bleached (unipolar dye). The tissue was then mounted on a coverslip and rinsed with fresh Ames solution for 15 min, allowing for unbound DAF to be cleared from the tissue. In our first set of experiments, DAF fluorescence was observed in darkness, constant bright illumination, 3 Hz light flicker, or in the presence of NO donor SNAP. In our second set of experiments, nNOS-2 ACs were depolarized by either whole cell or perforated patch access delivering current injections of 100-200 pA at  $\sim$ 3 Hz. Perforated patch access utilized electrodes that were front-filled with regular  $K^+$ -based intracellular solution and back-filled the same solution with 180  $\mu$ M amphotericin (Sigma-Aldrich). nNOS-2 ACs were also depolarized in presence of NOS inhibitor L-NAME (150  $\mu$ M perfused for 10 min prior to current injection). Light stimuli or depolarizing current pulses were followed immediately by tissue fixation and imaging with confocal microscopy. When imaging DAF-stained retina with confocal microscopy, image acquisition settings were maintained across tissues in order to compare and quantify increases in DAF fluorescence between cells and experiments. Whether the cells were stimulated with light or depolarization, experiments were performed in parallel using both retinas from the same mouse on two different electrophysiology rigs.

### Tracer coupling

For tracer coupling experiments, target cells were injected with  $K^+$ -based internal solution containing 3% neurobiotin and subsequently labeled with streptavidin. To label and image tissue with an intended reduction in the degree of nNOS-2 network coupling, neurobiotin was introduced via patch electrode after exposure to (1) the exogenous NO donor S-nitroso-N-acetylpenicillamine (SNAP; 100  $\mu$ M for 45 min), (2) gap junction blocker meclofenamic acid (MFA; 100  $\mu$ M for 25 min), or (3) a full-field light flicker protocol (darkness to 50,000 R\*/rod/s for 45 min), or (4) a full-field light flicker protocol in presence of NOS inhibitor L-NAME (150  $\mu$ M perfused for 10 min prior to light flicker). Tissues were then fixed, mounted, and imaged with an inverted 40x or 60x oil immersion lens (Nikon Plan Apo VC x40/x60/1.4 NA) on a Nikon A1R laser scanning confocal microscope equipped with Nikon Ti ZDrive PerfectFocus and emitted fluorescence was collected via GaAsP detectors. During confocal imaging acquisition, large areas were often scanned to collect the entirety of these broadly coupled neural networks (1000  $\times$  1000  $\mu$ m, 5  $\times$  5 stitched image windows). Streptavidin-conjugated fluorescent labeling was excited at 488 nm, tdTomato was excited at 568 nm, and each channel was acquired in 0.5-1  $\mu$ m steps in the z axis. All confocal imaging was performed at the Nikon Imaging Center at Northwestern University's Feinberg School of Medicine using Nikon Elements software.

### Immunohistochemistry

Tissues were fixed for 30 mins in 4% paraformaldehyde (Electron Microscopy Sciences) and incubated in 0.1 M phosphate buffer (PB) overnight at 4°C. Fixed retinas were incubated in blocking solution (phosphate-buffered saline; PBS) containing 3% normal donkey serum (blocking agent), 0.05% sodium azide, 0.5% Triton x 100 for 2 hr. This was followed by incubation in blocking solution and primary antibody against one of the following; nNOS (ThermoFisher Scientific, 61-7000, rabbit anti-nNOS, 1:1000 v/v), sGC  $\beta$ -1 subunit (Santa Cruz, sc-514183, mouse anti-sGC, 1:250 v/v), ChAT (Millipore, AB144P, goat anti-ChAT, 1:500 v/v), PSD-95 (Cell Signaling Technology, D27E11, rabbit anti-PSD-95), Cx36 (ThermoFisher Scientific, 51-6200, mouse anti-Cx45, 1:100 v/v), or Cx45 (ThermoFisher Scientific, 41-5800, mouse anti-Cx45, 1:100 v/v) for 5 nights at 4°C. Afterward, tissues were rinsed in 0.1 M PB and incubated for 2 nights at 4°C with secondary antibody against rabbit IgG (Jackson ImmunoResearch, 711-605-152, donkey anti-rabbit Alexa Fluor 647, 1:250 v/v) or mouse IgG (Life Technologies, A-31571, donkey anti-mouse Alexa Fluor 647, 1:250 v/v) or goat IgG (Jackson ImmunoResearch, 711-605-152, donkey anti-goat Alexa 647, 1:500 v/v) and streptavidin (ThermoFisher Scientific, 21832, DyLight 488, 1:500 v/v). Following immunostaining, retinas were mounted on slides with Vectashield Antifade mounting (Vector Labs) medium and imaged with Nikon A1R laser scanning confocal microscope.

### Biophysical network model

We generated an abstract anatomical model of nNOS-2 ACs in MATLAB based on prominent geometrical features in the cells we observed, with the intention not of precisely recreating the observed networks, but of constructing a network that might occur naturally. All parameters of the model are listed in Table S1 along with our methods for estimating their values.

First, we took anatomical measurements from traced nNOS-2 ACs to create a cable model of an individual cell isolated from the network (Figure S7A). Fitting the single parameter of membrane resistivity allowed our cable model to match the largely passive electrical properties of nNOS-2 ACs pharmacologically isolated with MFA (Figure S7B). Models of either individual traced cells or our abstracted morphological model captured both the time constant and input resistance of MFA-isolated cells with this one-parameter fit (Figures S7C and S7D). Our passive model deviated from the data in the sustained phase (after 100 ms) for the largest depolarizations (Figures S7B and S7D), but we chose not to model the current(s) responsible for this systematic deviation because they are unlikely to affect  $\text{Ca}^{2+}$  influx, which occurs on a faster timescale (Figures S3C and S3D).

In the network model 36 cells were tiled in a hexagonal grid with an average spacing of 125  $\mu\text{m}$  and assigned a stereotyped morphology as observed here and in Zhu et al., 2014 with 4 to 6 neurite processes made to extend 1300  $\mu\text{m}$  each. Gap junctions were randomly assigned to some of the intersecting processes in accordance with a desired density.

This anatomical information was imported into NEURON (Hines and Carnevale, 1997), where additional anatomical and biophysical properties were incorporated into the model. The soma and primary neurites were approximated as cylinders with lengths of 12  $\mu\text{m}$  and 40  $\mu\text{m}$  and diameters of 12  $\mu\text{m}$  and 2  $\mu\text{m}$ , respectively, whereas daughter neurites were assigned randomly varying thicknesses with an average diameter of 1  $\mu\text{m}$ . The specific capacitance of the membrane ( $C_m$ ) and the cytoplasmic resistivity ( $R_i$ ) were assigned standard values of 1  $\mu\text{F}/\text{cm}^2$  and 110  $\Omega\text{-cm}$ , respectively (Olstedal et al., 2009; Rempe et al., 2008). Gap junction conductance was initially set to zero so that the membrane resistivity ( $R_m$ ) could be estimated using the input resistance of nNOS-2 ACs under MFA (Figure 6G). Gap junction conductance was then modulated to recreate the input resistances observed under varying experimental conditions (Figure 8D).

To probe the relationship between gap junction coupling and individual synaptic events on the neurites, we modeled synaptic stimulation as occurring uniformly within a circle 40  $\mu\text{m}$  in diameter at various locations in the network (Figure S8). This is the size of  $\sim 1$ -3 bipolar cell axon terminals and approximately the receptive field size of a single bipolar cell (Bertson and Taylor, 2000; Schwartz et al., 2012; Wässle et al., 2009), so it is a reasonable approximation of the stimulation area for a small spot of light. All neurites passing through the stimulus area were activated by synapses at 6.5  $\mu\text{m}$  intervals (Jakobs et al., 2008). We injected a 100 ms step of 10 pA of current at each synapse. We modeled the spread of voltage throughout the network, and we plot the maximum depolarization at each spatial location in Figures S8A and S8B. We computed normalized  $\text{Ca}^{2+}$  influx by passing our voltage values through the sigmoidal function we plot in Figure 4G. Model code in NEURON and MATLAB is available at <https://github.com/SchwartzNU/SymphonyAnalysis>.

## QUANTIFICATION AND STATISTICAL ANALYSIS

### Statistical analysis

Data are reported as mean  $\pm$  SEM except where noted (SD in Figure 8D). Statistical tests used to test significance are mentioned in the text or figure legends along with the number of data points. No statistical methods were used to predetermine sample sizes. Data collection was randomized across conditions of the experiments.

### Physiology analysis

Data were analyzed with a custom open-source MATLAB analysis package (<https://github.com/SchwartzNU/SymphonyAnalysis>) and figures were assembled in Igor Pro and Adobe Illustrator. Sigmoid fits of  $\text{Ca}^{2+}$  influx (Figures 4D and 4G) used the equation:

$$\text{Ca}^{2+} = \frac{1}{1 + e^{\frac{V_1 - V}{\alpha}}}$$

in which the relative  $\text{Ca}^{2+}$  influx is a function of the voltage ( $V$ ) parameterized by the half-maximal voltage,  $V_{1/2}$ , and the slope,  $\alpha$ . Coupling coefficients (Figure 2E) and input resistance measurements (Figure 6G) used the average, steady-state voltage in the last 100 ms of each 500 ms current step. Coupling coefficients were computed as the ratio of the voltage change in the coupled cell to that in the injected cell. Input resistances were computed as the ratio of the voltage change to the amplitude of the current injection. In both cases, we took the average value over the linear range of both positive and negative current injection amplitudes.

### Image analysis

Images were analyzed using ImageJ/FIJI or MATLAB. Cells were traced using the Simple Neurite Tracer FIJI plugin. Analysis of sGC colocalization with nNOS-2 AC neurites was performed with custom written MATLAB software (<https://github.com/SchwartzNU/SymphonyAnalysis>). First, neurites were thresholded with a binary mask in the 3D volume. For each pixel in the mask, fluorescence in the sGC channel was measured in the surrounding 4.5  $\mu\text{m}$  square in the same z-plane. The map in Figure S6B is the average of this map across all mask pixels. DAF images were analyzed with custom written MATLAB software to determine the spatial decay of the fluorescence signal along neurites (Figures 5 and S4). Starting at the soma, each neurite from the traced image was followed in 3D and its distance from the soma measured. We defined the background as the mean pixel value within a 4  $\mu\text{m}$  cube outside the mask of

the neurite. We defined the signal as the mean pixel value inside the mask of the neurite within the same cube. Values in Figure 5D are computed as  $(\text{signal} - \text{background})/\text{background}$ . Each fluorescence change was associated with the corresponding distance of the dendritic segment from the soma, and then averaged in bins of 5  $\mu\text{m}$ . Somatic DAF fluorescence were calculated by drawing ROIs around somas in FIJI. PSD-95 puncta were counted in FIJI with the 3D Objects Tracer plugin after applying a mask for the traced nNOS-2 AC neurite (Figure S6). The linear density map was computed by smoothing the inter-puncta distances along the neurite with a 50  $\mu\text{m}$  sliding window filter.

#### **DATA AND SOFTWARE AVAILABILITY**

All custom analysis scripts can be found on our Github repository (<https://github.com/SchwartzNU/SymphonyAnalysis>). Requests raw data can be directed to the Lead Contact, Gregory Schwartz ([greg.schwartz@northwestern.edu](mailto:greg.schwartz@northwestern.edu)).